

Wave Generation from Explosions in Cavities in Rock

**Cangli Liu
Thomas J. Ahrens**

**California Institute of Technology
Seismological Laboratory 252-21
1200 E. California Blvd
Pasadena, CA 91125**

30 June 1998

Final Report

**APPROVED FOR PUBLIC RELEASE; DISTRIBUTION IS
UNLIMITED.**



20021008 020

**AIR FORCE RESEARCH LABORATORY
Space Vehicles Directorate
29 Randolph Rd
AIR FORCE MATERIEL COMMAND
Hanscom AFB, MA 01731-3010**

SPONSORED BY
Air Force Technical Applications Center
Directorate of Nuclear Treaty Monitoring
Project Authorization T/5101

MONITORED BY
Air Force Research Laboratory
CONTRACT No. F19628-95-C-0115

The views and conclusions contained in this document are those of the authors and should not be interpreted as representing the official policies, either express or implied, of the Air Force or U.S. Government.

This technical report has been reviewed and is approved for publication.



JAMES C. BATTIS
Contract Manager



CHARLES P. PIKE, Deputy Director
Integration and Operations Division

This report has been reviewed by the ESD Public Affairs Office (PA) and is releasable to the National Technical Information Service (NTIS).

Qualified requestors may obtain copies from the Defense Technical Information Center. All others should apply to the National Technical Information Service.

If your address has changed, or you wish to be removed from the mailing list, or if the addressee is no longer employed by your organization, please notify AFRL/VSOS-IM, 29 Randolph Road, Hanscom AFB, MA 01731-3010. This will assist us in maintaining a current mailing list.

Do not return copies of the report unless contractual obligations or notices on a specific document requires that it be returned.

REPORT DOCUMENTATION PAGE

Form Approved
OMB No. 0704-0188

The public reporting burden for this collection of information is estimated to average 1 hour per response, including the time for reviewing instructions, searching existing data sources, gathering and maintaining the data needed, and completing and reviewing the collection of information. Send comments regarding this burden estimate or any other aspect of this collection of information, including suggestions for reducing the burden, to Department of Defense, Washington Headquarters Services, Directorate for Information Operations and Reports (0704-0188), 1215 Jefferson Davis Highway, Suite 1204, Arlington, VA 22202-4302. Respondents should be aware that notwithstanding any other provision of law, no person shall be subject to any penalty for failing to comply with a collection of information if it does not display a currently valid OMB control number.

PLEASE DO NOT RETURN YOUR FORM TO THE ABOVE ADDRESS.

1. REPORT DATE (DD-MM-YYYY) 30 June 1998			2. REPORT TYPE Scientific, Final		3. DATES COVERED (From - To) 16 Jun 95-30 Sep 97	
4. TITLE AND SUBTITLE Wave Generation from Explosions in Cavities in Rock			5a. CONTRACT NUMBER F19628-95-C-0115 5b. GRANT NUMBER 5c. PROGRAM ELEMENT NUMBER 35999F			
6. AUTHOR(S) Cangli Liu Thomas J. Ahrens			5d. PROJECT NUMBER 5101 5e. TASK NUMBER GM 5f. WORK UNIT NUMBER AH			
7. PERFORMING ORGANIZATION NAME(S) AND ADDRESS(ES) California Institute of Technology Seismological Laboratory 252-21 1200 E. California Blvd Pasadena, CA 91125					8. PERFORMING ORGANIZATION REPORT NUMBER	
9. SPONSORING/MONITORING AGENCY NAME(S) AND ADDRESS(ES) Air Force Research Laboratory/VSBI 29 Randolph Road Hanscom AFB, MA 01731-3010					10. SPONSOR/MONITOR'S ACRONYM(S) 11. SPONSOR/MONITOR'S REPORT NUMBER(S) AFRL-VS-HA-TR-98-0078	
12. DISTRIBUTION/AVAILABILITY STATEMENT Approved for Public Release; distribution unlimited.						
13. SUPPLEMENTARY NOTES						
14. ABSTRACT <p>We have developed a measurement method to monitor P- and S-waves generated from laboratory-scale explosions in meter-sized rock media at a series of stations, and invented a unique device to drill spherical cavities with diameters of up to 10 cm in rock. We have also conducted laboratory experiments in which spherical/cylindrical charges of 0.2 to 1.9 g mass were detonated at the center of spherical/cylindrical cavities with radii from 0.6 to 1.5 cm in Bedford limestone and the waves generated by the explosions were recorded in the near field within 250 mm. The records and post-explosion studies clearly demonstrate the P-waves generated from both explosions in cavities and crack propagation in rock. The peak particle displacement induced by P-waves ranges from 9 to 15 um at 150 to 210 mm from the source for the spherical cavity experiment with 1.9 g explosives, and 8 to 4 um at 150 to 220 mm from the source with 0.8 g explosives, 35 to 10 um at 150 to 240 mm for the tamped cylindrical cavity experiment with 1.2 g explosives and 7 to 2 um at 150 to 190 mm from the source for the decoupled cylindrical cavity experiment with 0.24 g explosives.</p>						
15. SUBJECT TERMS Confined explosions Limestone Discrimination Shear waves Pressure waves Cylindrical cavity Spherical cavity						
16. SECURITY CLASSIFICATION OF:			17. LIMITATION OF ABSTRACT UNL	18. NUMBER OF PAGES	19a. NAME OF RESPONSIBLE PERSON James Battis 19b. TELEPHONE NUMBER (Include area code) 781 377-4669	
a. REPORT UNC	b. ABSTRACT UNC	c. THIS PAGE UNC				

Contents

Abstract	1
1 Introduction	3
2 Measurement Method	6
2.1 Introduction	6
2.2 Sensors	6
2.3 Data Reduction Method	7
2.3.1 P-wave reflection at free surfaces	7
2.3.2 SV-wave reflection at free surfaces	8
2.3.3 Strains induced by incident P-waves	9
2.3.4 Strains induced by incident S-waves	11
2.3.5 Amplitudes of incident P- and S-waves	12
2.4 Characteristics of the Strains along the Two Directions	12
2.4.1 Strains induced by incident P-waves	12
2.4.2 Strains induced by incident S-waves	14
2.5 Conclusions	15
3 Wave Generation From Explosions in Spherical Cavities in Rock	16
3.1 Introduction	16
3.2 Experiments and Results	16
3.2.1 Spherical cavity drill	16
3.2.2 Experimental details	19
3.2.3 Experimental records	21
3.2.4 Crack pattern from the recovered samples	21
3.3 Analysis of the P-waves Induced by Explosions and Cracking	25
3.3.1 P-wave velocity	25
3.3.2 Particle displacement induced by P-waves	25
3.3.3 Comparison between experimental data and theoretical predictions	26
3.3.4 Comparison between the observation and theoretical predictions of displacement history induced by P-waves	38
3.3.5 P-wave decay	41

3.4	Analysis of the S-waves Generated from Explosions and Cracking	42
3.4.1	S-wave arrival	42
3.4.2	S-wave amplitudes	44
3.4.3	S-wave profiles generated from cracking	45
3.5	Conclusions	47
4	Wave Generation From Explosions in Cylindrical Cavities in Rock	50
4.1	Introduction	50
4.2	Experiments and Results	50
4.2.1	Experimental Details	50
4.2.2	Experimental Results	50
4.3	P-waves Generated from Explosions	53
4.3.1	P-waves generated from the decoupled experiment	53
4.3.2	P-waves generated from the tamped experiment	54
4.4	S-waves Generated from Explosion	54
4.4.1	S-waves generated from the decoupled experiment	54
4.4.2	S-waves generated from the tamped experiment	55
4.5	Conclusions	55
5	Summary	59
Bibliography		62

List of Figures

2.1 Sample and strain gauge layout for spherical cavity experiments	13
2.2 H and G versus incident angle	15
3.1 Schematic of spherical cavity drill	17
3.2 Assembly drawing of spherical cavity drill	18
3.3 Mechanical configuration of the test chamber.	20
3.4 Spherical explosive source arrangement.	21
3.5 Strain signals from all the gauges in SW4.	22
3.6 Strain signals from all the gauges in SW9.	22
3.7 Strain signals at the same location from the gauges in SW4 and SW9.	23
3.8 Strain signals at the same location from the gauges in SW4 and SW9.	24
3.9 Schematic of the large cracks in relation to the spherical cavity.	25
3.10 P-wave arrival versus radius.	26
3.11 P-wave particle displacement versus time for SW4.	27
3.12 P-wave particle displacement versus time for SW9.	27
3.13 Scaled maximum P-wave particle displacement versus propagation distance	28
3.14 Typical displacement history from the spherical model without cracking	30
3.15 Pressure history	39
3.16 Comparison between the experimental data and the results from the equivalent models	40
3.17 Peak P-wave induced particle displacement versus propagation distance	43
3.18 Maximum shear wave strain versus propagation distance	45
3.19 Maximum shear wave displacement versus propagation distance	46
3.20 Shear strain history	48
4.1 Sample and strain gauge layout for cylindrical cavity experiments	51
4.2 Experimental results of the decoupled explosion, Shot SW1	52
4.3 Experimental results of the tamped explosion, Shot SW2	53
4.4 P-wave amplitudes from decoupled experiment	53
4.5 P-wave generated from the tamped experiment	54
4.6 P-wave amplitude versus propagation distance for SW1 and SW2	55
4.7 Strain signals at different location for SW1	56
4.8 Strain signals at the different location for SW2.	57

4.9	S-wave amplitude versus propagation distance for SW1 and SW2	58
5.1	Possible damage difference between chemical and nuclear explosions	61

List of Tables

3.1 Data for spherical cavity experiments	20
4.1 Data for cylindrical cavity experiments	52

Abstract

We have developed a measurement method to monitor P- and S-waves generated from small laboratory-scale explosions in meter-sized rock media at a series of stations as well as invented a unique device to drill spherical cavities with the diameter up to 10 centimeters in rock.

We have also conducted laboratory experiments in which spherical/cylindrical charges in 0.2 to 1.9 gram mass range were detonated at the center of spherical/cylindrical cavities with the radius from 0.6 to 1.5 cm in Bedford limestone and the waves generated by explosions were recorded in the near field within 250 mm. The records and post-explosion studies clearly demonstrate the P-waves generated from both explosions in cavities and crack propagation in rock. The peak particle displacement induced by P-waves ranges from 9 to 5 μm at 150 to 210 mm from source for the spherical cavity experiment with 1.9 gram explosives, and 8 to 4 μm at 150 to 220 mm from source for spherical experiment with 0.8 gram explosives, 35 to 10 μm at 150 to 240 mm from source for the tamped cylindrical cavity experiment with 1.2 gram explosives and 7 to 2 μm at 150 to 190 mm from source for the decoupled cylindrical cavity experiment with 0.24 gram explosives. The step-like pressure model can be used to explain the experimental results on the peak P-wave induced particle displacement versus propagation distance from the explosions in spherical cavities but not in cylindrical cavities. This results demonstrates the cavity geometrical effects on wave pattern. The experimental results from both spherical and cylindrical cavities show that P-wave profiles are similar with each other. The experimental results verify that S-waves are generated from both shock wave-to-S conversion at cavity walls and crack propagation in rocks. The amplitude of S-waves from shock wave-to-S conversion is from 10 to 27 μm at 150 to 180 mm from source for the spherical experiment with 1.9 gram explosives, 8 to 21 μm at 150 to 180 mm from source for the spherical experiment with 0.8 gram explosives. The amplitude of S-waves generated by crack propagation is from 9 to 19 μm at 150 to 180 mm from source for the spherical ex-

periment with 1.9 gram explosives, 8 to 19 μm at 150 to 180 mm from source for the spherical experiment with 0.8 gram explosives. Based on the experimental data, the ratio of S-wave to P-wave amplitude is approximately about 2.

We have analyzed P and S-waves generated by explosions and crack propagation in rock. A theoretical model is proposed to explain the differences of P-wave induced displacement history between the observed waveforms and that predicted by a step pressure source. The predictions of this model fit the observation qualitatively. The present results demonstrate the important role of rock cracking in P and S-wave generations from overdriven cavities.

The results from this work have demonstrated that the seismic source for underground explosions in cavities is much more complex than seismic theoretical models used to describe underground explosions. The rich phenomena associated with waves generated from explosive product driven crack extending from cavities suggest that this research direction may lead to development of the criteria that can be used to discriminate underground explosions from earthquakes and possible discriminate chemical from nuclear explosion sources.

Chapter 1 Introduction

In the past 30 years, extensive research has been conducted on the discrimination of underground explosions from earthquakes. As a result, Murphy (1996) recently concluded that the seismology of earthquakes and underground explosions is at a state that it is possible to identify tamped explosions with a yield over 1 kiloton ($m_b \geq 4$) on a world-wide basis. These explosions can be distinguished from earthquakes by the global seismic stations using the initial P-wave motion and the M_s to m_b ratio. In fact, the discrimination of the tamped explosions from earthquakes depends mainly on the collection of seismic data from previous underground nuclear explosions. However, many basic problems related to tamped explosions still remain unsolved (Masse, 1981; Murphy, 1996), e.g., the generation of long-period Rayleigh waves (≥ 5 seconds), SH-waves and Love-waves etc. But now, the most difficult problems are to distinguish earthquakes from decoupled explosions with complex geometries and chemical explosions from small nuclear explosions.

The characteristics for decoupled explosions (Murphy, 1996) are: (1) m_b is too low to use the global monitoring system (in general, $m_b \leq 3$); (2) the amplitudes of surface waves generated from such explosions are much lower than from tamped explosions; (3) the excitation of direct SV-waves and possibly SH-waves makes the problem more difficult. Although there are many published papers related to decoupled explosions (Glenn et al., 1985, 1993, 1994, 1996; Murphy et al. 1996; Murphy, 1996; Sykes, 1996; Langston, 1983 etc.), it still is unclear what really controls the generation of S-waves from decoupled explosions (Murphy, 1996). We conclude that the mechanisms of S-wave generation from explosions, especially from decoupled explosions in cavity is potentially an important discrimination criterion.

The suggested possible sources for S-waves from explosions include:

1. dynamic fracture of rocks near explosions;
2. the asymmetric plastic deformation near the explosion due to the asymmetric

- geometry and anisotropy of the rocks;
3. tectonic release of shear energy triggered by shock waves from the explosions;
 4. the conversion of P-waves to S-waves at the free surface of the Earth;

These mechanisms must be studied separately using different methods.

The objective of this work is to investigate P- and S-wave generations from explosions in cavities, dynamic fracture in rock and the conversion of shock induced P- and S-waves at the surfaces of the cavities experimentally. If the shock wave pressure in cavity is not too high, the rocks near explosions will fail via brittle fracture mechanisms. Radial fractures may be initiated from the inner surface of the cavity because the tangential(hoop) stresses always achieve the maximum value at the surface. Radial fractures generally can be further driven by the high-pressure explosive products (Coursesn, 1985). The propagation of radial cracks may result in P- and S-wave generations. The reflection of the shock waves at cavity surfaces will also induce S-waves.

In order to investigate the details of the P- and S-wave generations from explosions in cavities in rock, a measurement method that has the capability to measure P- and S-waves generated from explosions in meter-size samples and a device that can form spherical cavities in rock have to be developed.

For small-scale laboratory experiments, the wave profiles have much higher frequencies than the usual seismic waves. Therefore, conventional seismic recording systems can not be used to measure those wave profiles. One candidate method developed for super-high strain rate experiments we considered (Kim and Clifton, 1977) is difficult to employ for the present experiments because it requires special treatment of sample surfaces. Magnetic velocity gauges have long been used to study shock wave decays in rocks, but this method requires embedding the gauges in the rock and thus contains considerable machining of rocks. This also adds some artificial internal interfaces which will generate S-waves and make the S-wave train more complicated. Based on the analysis of the interaction between P- and S-waves and free-surfaces, we have developed a method to measure P- and S-wave profiles on the free surfaces of rocks. The main idea of the method is to use the different characteristics of the

interactions between P- and S-waves and the free surface. In order to make a spherical cavity in rock, a special drilling tool has been developed and used in the experiments successfully.

In this report, the details of the method including measuremental method and spherical cavity drilling method are described. Experimental data on spherical and cylindrical cavities and the analysis on P- and S-wave profile and amplitudes are presented.

Chapter 2 Measurement Method

2.1 Introduction

When P- and S-waves arrive at a free surface, the interactions between the P- and S-waves and the free surface are very different. The characteristics of these interactions provide the opportunity to measure the incident P- and S-wave amplitudes from the strain measurements on the free surfaces of rocks. The method developed is to use two strain gauges to measure the strains along two perpendicular directions at one point on the free surface of rock. The incident amplitude of P- and S-waves can be obtained from these strain measurements.

The basic assumptions made for the method are:

1. The waves in the rocks can be approximately treated locally as plane waves because the dimensions of strain gauges used in experiments are only 3x3 mm and gauges are located at least 150 mm away from the explosive sources.
2. The deformation of the rocks near the free surface is elastic.

The following is the details of the derivation of the relations between the signals from strain gauges and P- and S-waves in rock.

2.2 Sensors

A group of strain gauges are employed to monitor the wave profiles at different locations along two directions on the free-surface of rock samples. The directions of the gauges are shown in figure 2.1. The gauges and amplifiers are powered by batteries in order to achieve a high signal to noise ratio. A mercury relay is used to calibrate the system. The relation between strains, ϵ , and the voltage change, ΔV , is

$$\epsilon = \frac{\Delta V}{fgV_0}, \quad (2.1)$$

where V_0 is the initial voltage supplied on the gauges. f and g are the gauge factor and gain of the amplifiers, respectively.

2.3 Data Reduction Method

Strain gauges give the elongation along the gauge directions. When they are attached on a free surface, they measure the elongation of the free-surface after wave reflections. The strains recorded by the gauges include the contributions from incident P- and S-waves and the reflected P- and S-waves. In order to get the relation between the strains given by the gauges and the incident P- and S-wave amplitudes, we first applied the well-known formulas describing the interactions between the incident P- and S-waves and the free surface.

2.3.1 P-wave reflection at free surfaces

The displacement reflection coefficients for incident P-waves at free surfaces (Aki and Richards, 1980) are

$$PP = \frac{B - A}{B + A}, \quad (2.2)$$

$$PS = \frac{2\beta \sin(2\theta) \cos(2j)}{A + B}, \quad (2.3)$$

where PP and PS are the reflection coefficients for P- and SV-wave displacements due to the incident P-waves, respectively. α and β are P- and S-wave velocities, respectively. A and B are

$$A = \cos^2(2j), \quad (2.4)$$

$$B = \left(\frac{\beta}{\alpha}\right)^2 \sin(2j) \sin(2\theta), \quad (2.5)$$

where θ and j (see 2.1) are the P-wave incident angle and S-wave reflection angle, respectively.

$$\sin j = \frac{\beta}{\alpha} \sin \theta, \quad (2.6)$$

$$\cos j = \left(1 - \left(\frac{\beta}{\alpha}\right)^2 \sin^2 j\right)^{\frac{1}{2}}. \quad (2.7)$$

The resultant displacements of the particles on the free surfaces after the reflection are

$$u_{par}^p = u_p^I[(1 + PP) \sin \theta + PS \cos j] = H_{par} u_p^I, \quad (2.8)$$

$$u_{per}^p = u_p^I[(1 - PP) \cos \theta + PS \sin j] = H_{per} u_p^I, \quad (2.9)$$

where u_p^I is the particle displacement of the incident P-wave, u_{par}^p and u_{per}^p indicate the resultant particle displacements along direction 2 and the direction that is perpendicular to the free surface after reflection as shown in figure 2.1, respectively. The H_{par} and H_{per} are

$$H_{par} = (1 + PP) \sin \theta + PS \cos j, \quad (2.10)$$

$$H_{per} = (1 - PP) \cos \theta + PS \sin j. \quad (2.11)$$

Substituting PP with Eq.(2.2) and PS with Eq.(2.3), Eqs.(2.10) and (2.11) can be rewritten as

$$H_{par} = \frac{2 \cos \theta \sin(2j)}{A + B}, \quad (2.12)$$

$$H_{per} = \frac{2 \cos \theta \cos(2j)}{A + B}. \quad (2.13)$$

2.3.2 SV-wave reflection at free surfaces

For incident SV-waves, the displacement reflection coefficients for P- and SV-waves (Aki and Richards, 1980) are

$$SP = \frac{\frac{\beta}{\alpha} \sin(4\theta)}{A_s + B_s}, \quad (2.14)$$

$$SS = \frac{A_s - B_s}{A_s + B_s}, \quad (2.15)$$

where SS and SP are the reflection coefficients of SV- and P-wave displacements due to the incident SV-waves.

$$A_s = \cos^2(2\theta), \quad (2.16)$$

$$B_s = \left(\frac{\beta}{\alpha}\right)^2 \sin(2\theta) \sin(2j), \quad (2.17)$$

where θ and j are the SV-wave incident angle and P-wave reflected angle, respectively, and

$$\cos j = (1 - (\frac{\alpha}{\beta})^2 \sin^2 \theta)^{\frac{1}{2}}. \quad (2.18)$$

The resultant displacements of the particles on the free surfaces after the reflection are

$$u_{par}^{sv} = u_{sv}^I [(1 + SS) \cos \theta + SP \sin j] = G_{par} u_{sv}^I, \quad (2.19)$$

$$u_{per}^{sv} = u_{sv}^I [(SS - 1) \sin \theta - SP \cos j] = G_{per} u_{sv}^I, \quad (2.20)$$

where u_{par}^{sv} and u_{per}^{sv} are the resultant particle displacements on the free surface after reflection along direction 2 as shown in figure 2.1 and the direction that is perpendicular to the free surface, respectively. u_{sv}^I is the particle displacement of the incident SV-wave. The G_{per} and G_{par} are

$$G_{par} = (1 + SS) \cos \theta + SP \sin j, \quad (2.21)$$

$$G_{per} = (SS - 1) \sin \theta - SP \cos j. \quad (2.22)$$

Substituting SP with Eq.(2.19) and SS with Eq.(2.15), Eqs.(2.21) and (2.22) are rewritten as

$$G_{par} = \frac{2 \cos(2\theta) \cos \theta}{A_s + B_s}, \quad (2.23)$$

$$G_{per} = -2 \frac{\frac{\beta}{\alpha} \cos j \sin(2\theta)}{A_s + B_s}. \quad (2.24)$$

2.3.3 Strains induced by incident P-waves

1. Strains measured along 1 direction

Because u_{per}^p is perpendicular to the free surface and along the symmetrical axis direction of the waves, the strain due to u_{per}^p along the 1 direction is

$$\varepsilon_1^{per} = \frac{H_{per}}{r_0} u_p^I, \quad (2.25)$$

where ε_1^{per} is the strain along direction 1 induced by u_{per}^p , and r_0 is the distance from the center of the cavity to the free surface at $\theta = 0$.

Because u_{par}^p does not result in any strains in the gauges along direction 1 at any time, the total strain induced by the incident P-waves is

$$\varepsilon_1^p = H_1 \frac{u_p^I}{r_0}, \quad (2.26)$$

where $H_1 = H_{per}$.

2. Strains measured along 2 direction

Because u_{per}^p and u_{par}^p all have contributions to the strain measured by gauges along the 2 direction, we need to consider the resultant displacements.

The length of the gauge after the reflection, l_s^r , is

$$l_s^r = (r_n^2 + (\frac{\partial r_n}{\partial \theta})^2)^{\frac{1}{2}} \delta\theta, \quad (2.27)$$

where

$$\delta\theta = \frac{l_s}{r_n}, \quad (2.28)$$

and l_s is the initial length of strain gauges. r_n is the distance from the center of the cavity to the position of the gauge after reflections

$$r_n = r + u \cos(\eta - \theta), \quad (2.29)$$

where r is the distance from the center of the cavity to the gauge before P-wave reflection, u is the resultant displacement of the point at θ on the free surface and η is the angle between u and u_{per}^p , they are

$$u = u_p^I \frac{2 \cos(\theta)}{A + B}, \quad (2.30)$$

$$\eta = 2j. \quad (2.31)$$

To a first-order approximation, l_s^r , is

$$l_s^r \approx ((\frac{r}{\cos \theta})^2 + 2ru_p^I(W(\theta) + \tan(\theta) \frac{dW}{d\theta}))^{\frac{1}{2}} \frac{l_s \cos \theta}{r}, \quad (2.32)$$

where

$$W = \frac{2 \cos(\theta) \cos(\eta - \theta)}{A + B}. \quad (2.33)$$

If $x \ll 1$, we have

$$(1 + x)^{\frac{1}{2}} \simeq 1 + \frac{x}{2}. \quad (2.34)$$

Because $u_p^I/r \ll 1$, after using the approximation above, l_s^r is

$$l_s^r \approx \left(r \left(1 + \frac{\tan^2 \theta}{2} \right) + u_p^I \left(W(\theta) \left(1 - \frac{\tan^2 \theta}{2} \right) + \tan \theta \frac{dW}{d\theta} \right) \right) \delta \theta. \quad (2.35)$$

Then the strain is

$$\varepsilon_2^p = \frac{l_s^r - l_s}{l_s}, \quad (2.36)$$

and therefore

$$\varepsilon_2^p = H_2 \frac{u_p^I}{r_0}, \quad (2.37)$$

where

$$H_2 = \frac{\left(\cos \theta \left(W \left(1 - \frac{\tan^2 \theta}{2} \right) + \tan \theta \frac{dW}{d\theta} \right) \right)}{\left(1 + \frac{\tan^2 \theta}{2} \right)}, \quad (2.38)$$

and $r_0 = r \cos \theta$.

2.3.4 Strains induced by incident S-waves

Using the same method, all the strains induced by incident SV-waves can be obtained.

The final expressions are listed as following:

1. Strains measured by gauges along 1 direction are

$$\varepsilon_1^{sv} = G_1 \frac{u_{sv}^I}{r_0}, \quad (2.39)$$

where

$$G_1 = G_{per}. \quad (2.40)$$

2. The strains given by the gauges along direction 2 can be found using the same method as for the incident P-wave. The resultant strains induced by the incident

SV-waves along direction 2 are

$$\varepsilon_2^{sv} = G_2 \frac{u_{sv}^I}{r_0}, \quad (2.41)$$

where

$$G_2 = \frac{\left(\cos \theta (W_s (1 - \frac{\tan^2 \theta}{2}) + \tan \theta \frac{dW_s}{d\theta})\right)}{\left(1 + \frac{\tan^2 \theta}{2}\right)}, \quad (2.42)$$

$$W_s = \frac{2 \cos(\eta - \theta) \cos \theta}{A_s + B_s} (\cos^2(2\theta) + 4(\frac{\beta}{\alpha})^2 \cos^2 j \sin^2 \theta)^{\frac{1}{2}}, \quad (2.43)$$

$$\tan \eta = -\frac{\alpha \cos \theta}{\beta \cos j \tan(2\theta)}. \quad (2.44)$$

2.3.5 Amplitudes of incident P- and S-waves

From the expressions given above, the displacements of incident P- and SV-waves can be obtained through the strains given by the gauges along the two directions.

1. The displacement of the incident P-waves is

$$u_p^I = r_0 \frac{\varepsilon_1^p}{H_1} = r_0 \frac{\varepsilon_2^p}{H_2}. \quad (2.45)$$

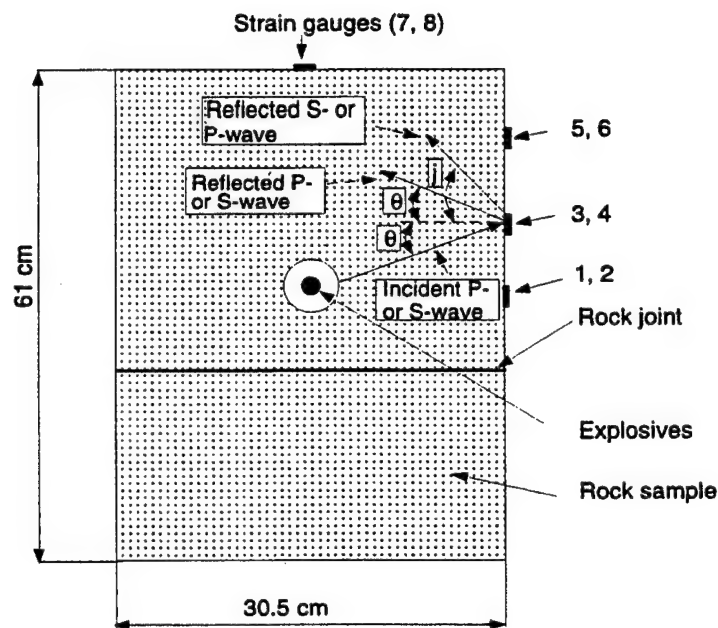
2. The displacement of the incident SV-waves is

$$u_{sv}^I = r_0 \frac{\varepsilon_{sv}^1}{G_1} = r_0 \frac{\varepsilon_{sv}^2}{G_2}. \quad (2.46)$$

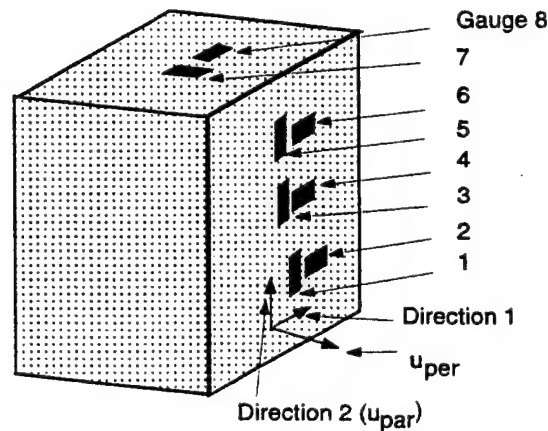
2.4 Characteristics of the Strains along the Two Directions

2.4.1 Strains induced by incident P-waves

1. The non-dimensional constant, H_1 in Eq.(2.45) is not sensitive to the variation in θ , e.g., the value of H_1 is about 2.0 for Bedford limestone. The non-dimensional constant, H_2 , in Eq.(2.45) changes rapidly with θ , it varies from about 2 to about -0.8 when incident angle changes from 0 to 55° for Bedford limestone as shown in figure 2.2.



(A) Layout of rock sample, strain gauges and explosive charge



(B) Sketch of polarization directions of strain gauges

Figure 2.1: Sample and strain gauge layout for spherical cavity experiments

2. From figure 2.2, the strains induced by P-waves along direction 1 are always positive, but the strains along direction 2 are positive when θ is less than 47° and negative when θ is larger than 47° (for Bedford limestone). This polarity change is controlled by the ratio of the projection of P-wave displacement along direction 1 to that along the direction that is perpendicular to the free surface.
3. The characteristics of the strain induced by incident P-waves have been verified by the experimental results as shown in figures 3.5, 3.6, 4.7 and 4.8. From the experimental results, it is seen that all the strains along direction 1 (labeled with even gauge number) are positive at all the stations and the strains along direction 2 (labeled with odd gauge number) are positive when the incident angle is smaller than the critical angle and negative when the incident angle is larger than the critical angle.

2.4.2 Strains induced by incident S-waves

1. The relation between G_1 (G_2) and the SV-wave incident angle for Bedford limestone is given in figure 2.2. From the calculated results, the gauges along direction 1 are not sensitive to incident SV-wave; however, the gauges along direction 2 are very sensitive to incident SV-wave.
2. The measurement of SV-waves are limited by the Rayleigh surface wave generation. For Bedford limestone, the Rayleigh wave is generated when θ is larger than about 35° (determined from Snell's law).
3. The polarities of the strains along direction 2 are negative, and the polarities of the strains along direction 1 are determined by the direction of the particle motion (the calculation is made assuming that the motion direction is toward the increasing direction of the SV-wave incident angle).
4. The characteristics of the strain induced by incident S-waves have been verified by the experimental results as shown in figures 3.5, 3.6, 4.7 and 4.8. From the experimental results, it is seen that all the strains along direction 1 (labeled with even gauge number) are generally very small compared to the correspond strain

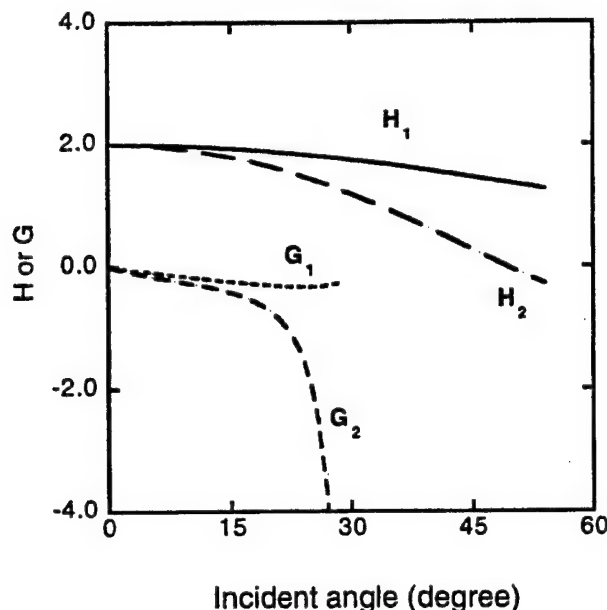


Figure 2.2: H and G versus incident angle

amplitudes along direction 2 at all the stations and the strains along direction 2 (labeled with odd gauge number) are always negative at all the stations.

2.5 Conclusions

A measurement method that can be used to monitor P- and S-waves generated from explosions has been developed. The relations between incident P and S-wave particle displacement and the strains recorded along the two directions have been derived as given in Eqs.(2.45) and (2.46) and the experimental set-up is shown in figures 2.1 and 3.3. Experimental results have verified the P- and S-wave characteristics predicted from the derived relations as shown in figure 2.2.

Chapter 3 Wave Generation From Explosions in Spherical Cavities in Rock

3.1 Introduction

Nearly all the seismic models for underground explosions assumed that the source is spherical (Murphy, 1996). Therefore, experimental study on the P and S-waves generated from the explosions in spherical cavities has direct applications to the understand of the waves from underground explosions. The objectives of this part is to study the P and S-waves generated from explosions in spherical cavities and also from crack propagation driven by shock waves and the explosive products.

3.2 Experiments and Results

3.2.1 Spherical cavity drill

In order to drill spherical cavities in rock, a special tool has been developed. The device is schematically shown in figure 3.1. Figure 3.2 is the assembly drawing of the drill. The principal of the drill is to use one of the two shanks, Shank A, to transfer the force from the machine to the other shank, Shank B, that rotates the blade and at same time push the blade to cut rock. During drilling process, the positioning plate is used to keep the drill from vibration induced by the asymmetrical force acting on the shank from blade. Pressurized air is used to cool the blade and also blow out the rock dust. Principally, the device can be used to drill spherical cavities with the diameter up to 10 centimeters in rocks like limestone. The procedures to form a spherical cavity inside rock are

1. We make a cylindrical hole with 1 cm diameter using a drill. The depth of the hole will be the deepest point of the spherical cavity.
2. After drilling, a small size blade with 1.5 cm diameter is put into the cylindrical

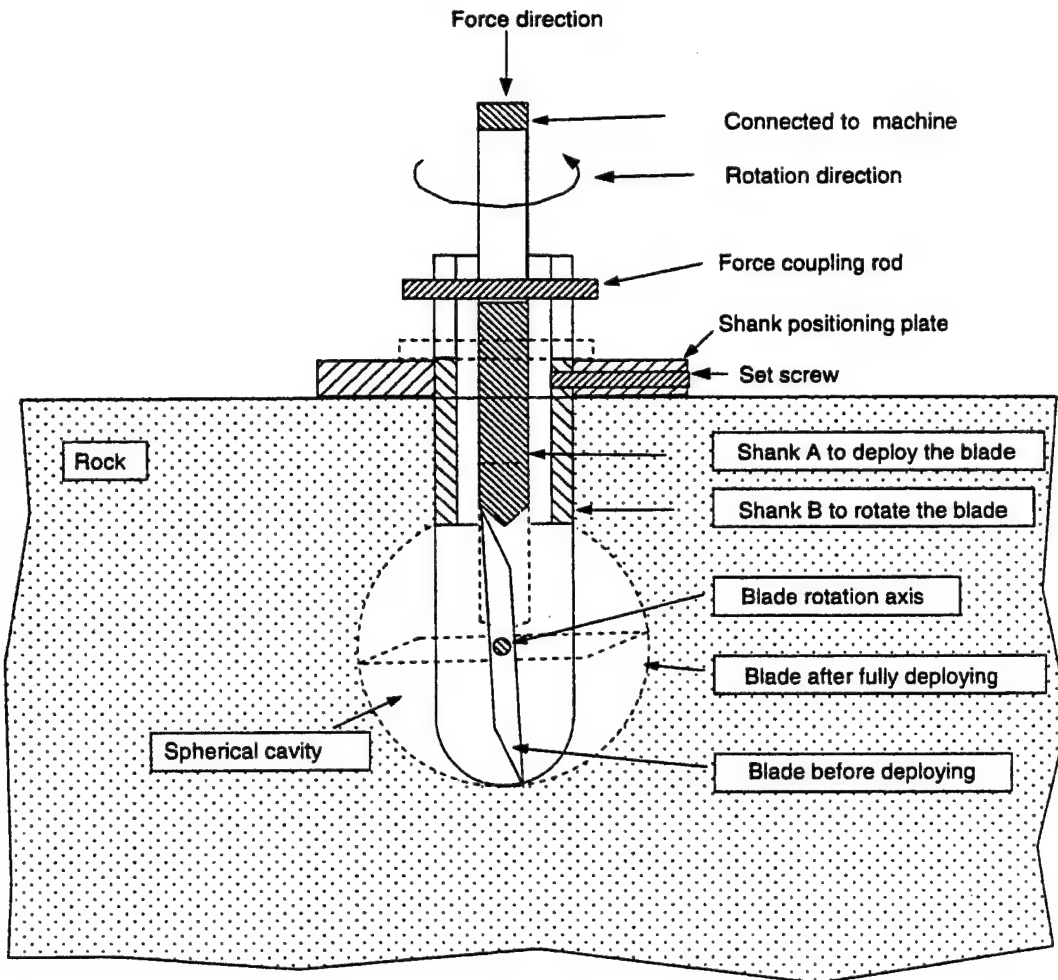


Figure 3.1: Schematic of spherical cavity drill

hole, the position plate is screwed to the shank to fix the depth of the spherical cavity and the center line in the rock target.

3. During drilling, pressurized air is used to blow out rock dust and also cool the blade. The air flow rate is roughly about 2 l/min. The rotation speed is about 240 r.p.m. and the feed rate is about 1 mm/min.
4. Then, a large blade is used to enlarge the cavity.

The device and procedure have been used to make spherical cavities in limestone successfully.

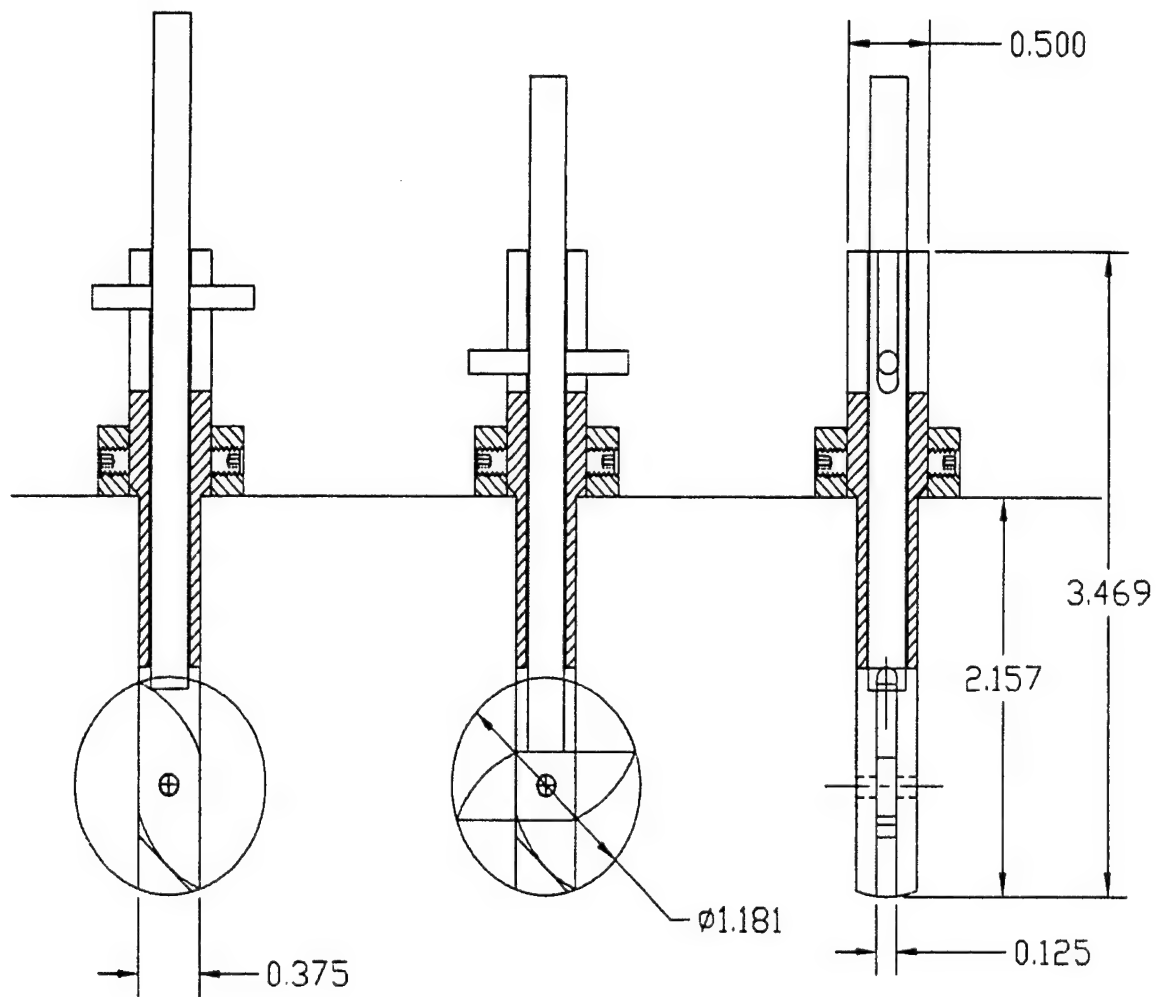


Figure 3.2: Assembly drawing of spherical cavity drill
Blade material: heat treated tool steel
Shank material: steel
Dimension unit: in

3.2.2 Experimental details

The rock sample (Bedford limestone) is assembled using two blocks as shown in figure 2.1. The rock sample with strain gauges is placed inside a tank pressurized to 10 bar. The type of strain gauge used in this work is CEA-00-062UT-120 from Measurements Group. The dimensions of the gauges are 3x3 mm. The initial resistance of gauges is $120 \Omega \pm 0.4\%$ and the gauge factor is $2.090 \pm 0.5\%$. The procedure to attach the gauges on the surface is: (1) The surface is polished with #240 sandpaper ; (2) the surface is cleaned using acetone; (3) the gauges are attached on the surface using 910 adhesive (Permabond International); (4) after the adhesive is dried, a thin layer of the epoxy (5-minute epoxy, ITWDevcon) is applied on the gauge surface in order to protect them. The voltage on the gauge is typical 6 V (before each experiment, the voltage on each gauge is measured). The amplifiers used in this work are specially designed to satisfy the requirements of high gain, wide bandwidth and low noise.

The explosives used in this work are Deta sheet PETN (DuPont) and Pellet pressed PETN (Reynolds Industries System Incorporated), the initial density is 1.5 gram/cm^3 for Deta sheet PETN and 1.4 gram/cm^3 for Pellet pressed PETN. The size of the detonator(Reynolds Industries System Incorporated) is $\phi 2 \times 8 \text{ mm}$.

We have fired several decoupled explosion tests in spherical cavities. Due to inherent difficulty to properly detonate small charge, we put much effort in completing a very few, highly successful experiments. The experimental setup is sketched in figures 2.1 and 3.3. Figure 3.4 schematically shows the spherical explosive source. Table 3.1 lists the parameters for 6 shots and the equilibrium pressure, p , in cavities estimated using the expression(Murphrey, 1961)

$$p = \frac{(\gamma - 1)E}{V}, \quad (3.1)$$

where γ is the ratio of specific heats of explosive products in air, E is the total energy of explosives used, V is cavity volume. In the calculation, γ is 1.4 (Baker, 1973) and the energy released from PETN is 1255 J/g (Dobratz, 1974).

Table 3.1: Data for spherical cavity experiments

Shot number	Explosive mass (gram.)	p (bar)
SW4	1.9	675
SW5*	0.4	142
SW6*	0.6	213
SW7*	0.7	248
SW8 *	0.8	284
SW9	0.8	284

* – indicates that the explosives did not properly detonate.

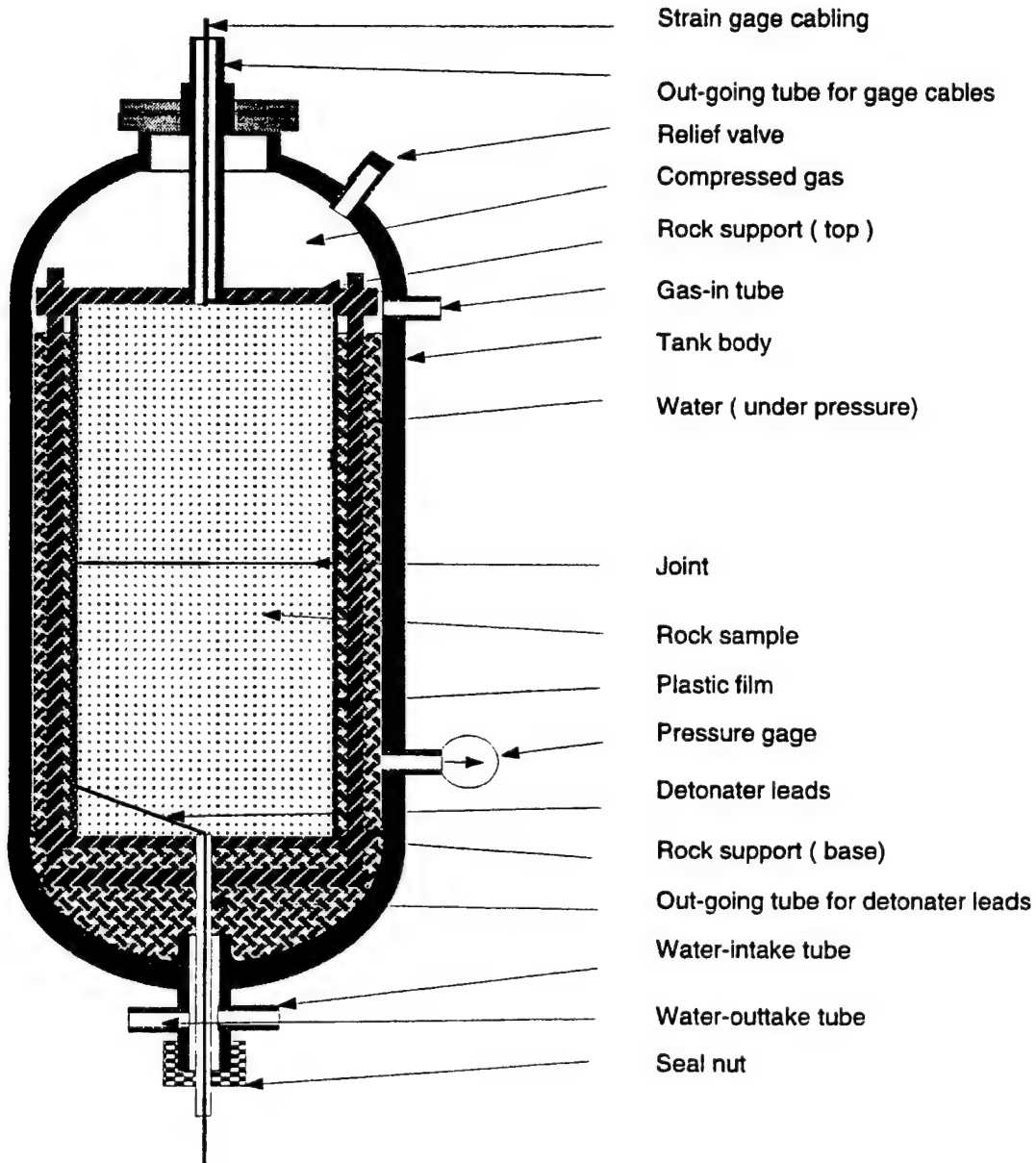


Figure 3.3: Mechanical configuration of the test chamber.

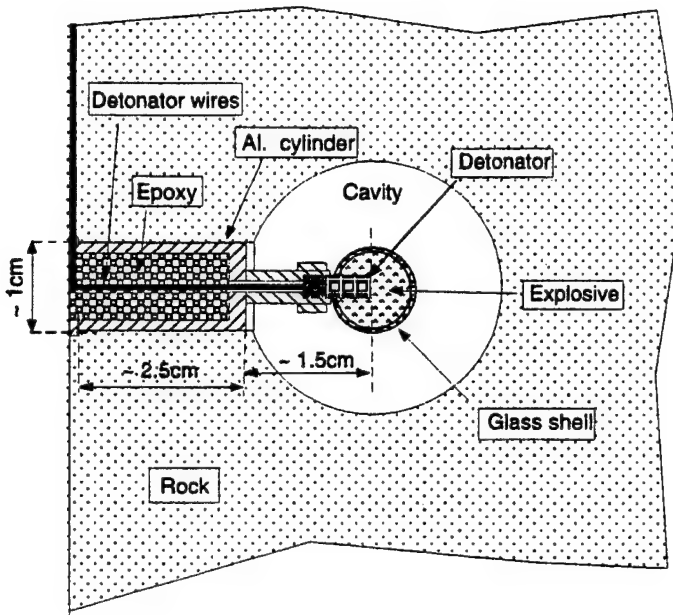


Figure 3.4: Spherical explosive source arrangement.

3.2.3 Experimental records

Using the experimental system given above and the measurement method described in Chapter 2, the waves generated from the explosions in spherical cavity were recorded. Experimental records along the two directions are shown in figure 3.5 for SW4 and figure 3.6 for SW9. The comparisons between the records at different locations are shown in figures 3.7 and 3.8.

3.2.4 Crack pattern from the recovered samples

(a) SW4

The recovered experimental sample shows that there are four large cracks (~ 10 cm) and many small cracks (~ 5 mm) induced by the explosion (Fig. 3.11). The length of the cracks with the explosion product trace ranges from 50 mm to 80 mm.

(b) Shot SW9

From the recovered sample, cracks were not seen from the free surfaces. After the sample was cut along the axis, many small cracks near the cavity existed and also two very long cracks are formed. The longest cracks are about 50 mm in length.

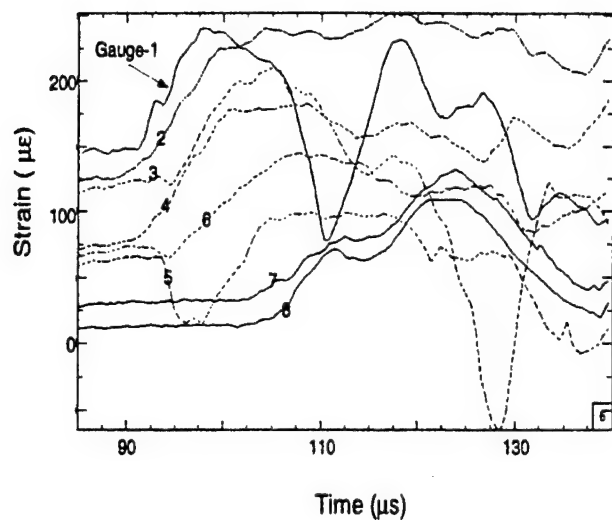


Figure 3.5: Strain signals from all the gauges in SW4.

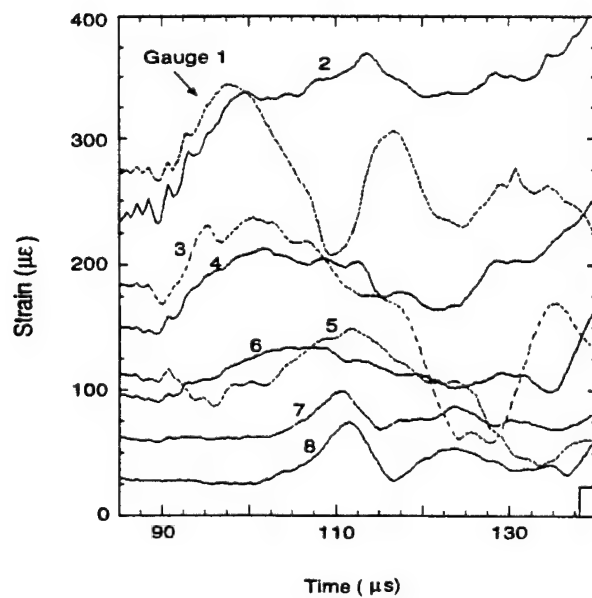


Figure 3.6: Strain signals from all the gauges in SW9.

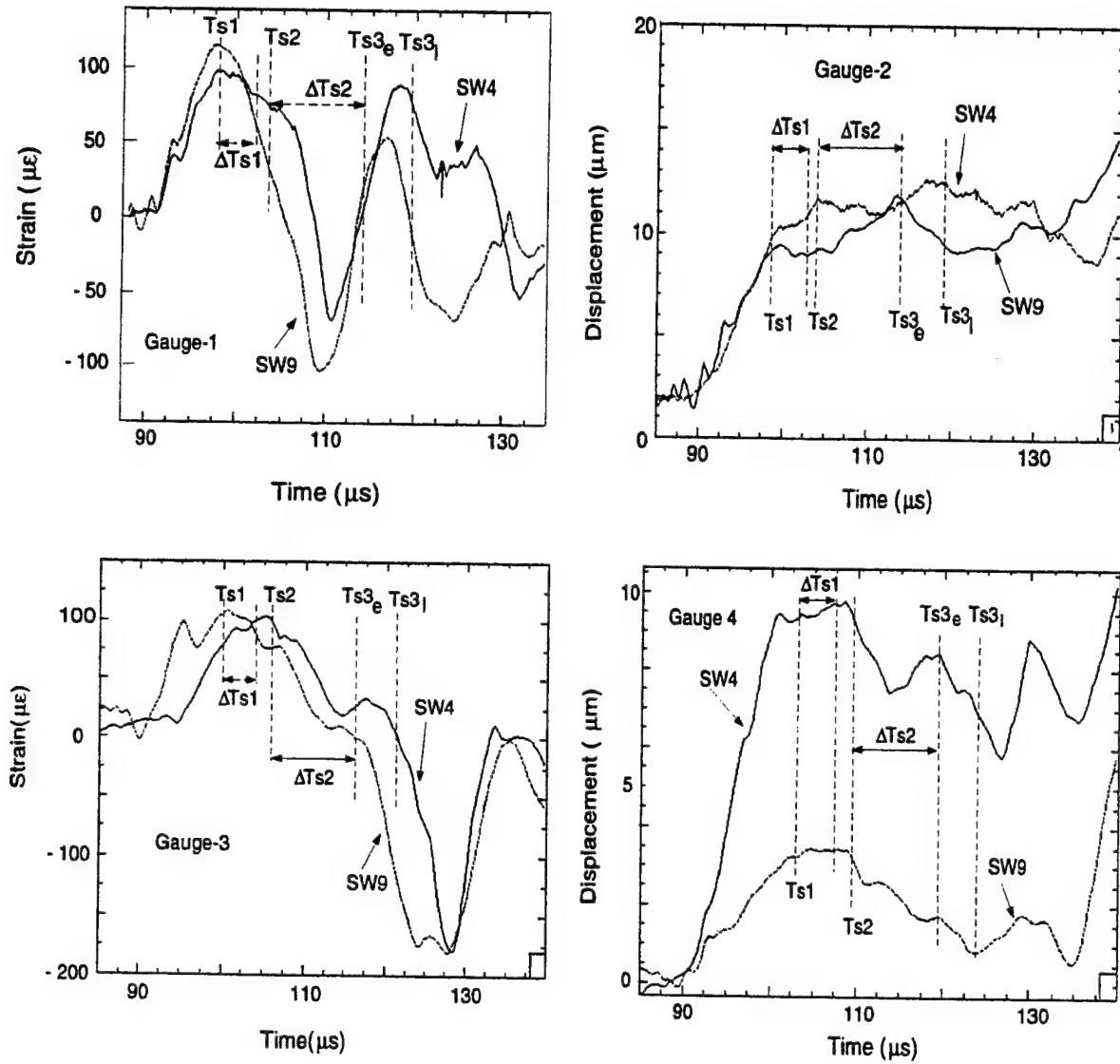


Figure 3.7: Strain signals at the same location from the gauges in SW4 and SW9.

- Ts1 and ΔTs_1 : the arrival and duration of the shear waves induced by microcracking (Eqs.(3.83) and (3.84))
- Ts2 and ΔTs_2 : the arrival and duration of the shear waves induced by shock wave-to-S conversion at the cavity wall (Eq.(3.82))
- Ts3_e and Ts3_i: the possible earliest and last arrival of the shear waves induced by macrocracking (Eqs.(3.86) and (3.87))

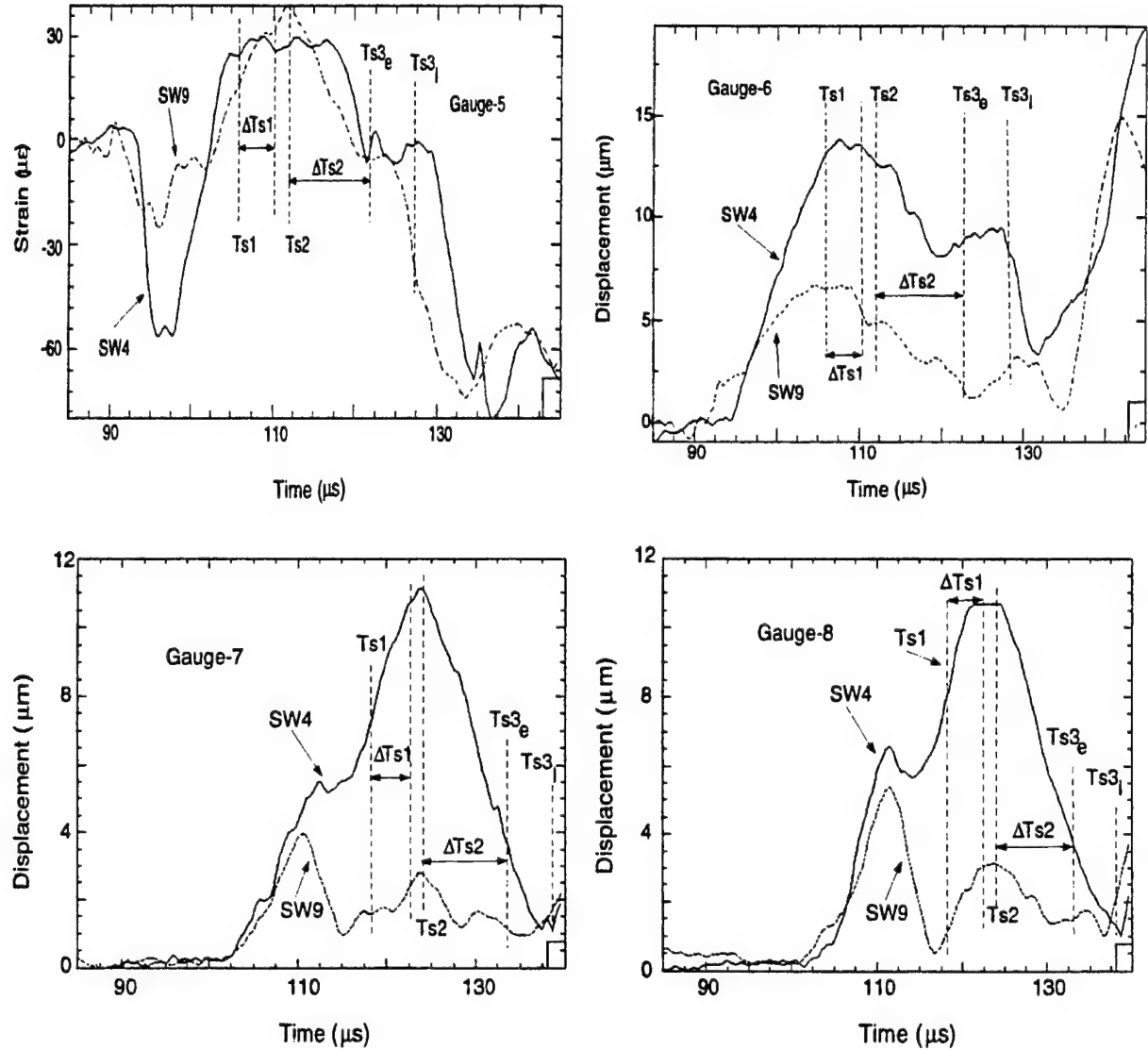


Figure 3.8: Strain signals at the same location from the gauges in SW4 and SW9.
Ts1 and ΔT_{s1} : the arrival and duration of the shear waves induced by microcracking (Eqs.(3.83) and (3.84))
Ts2 and ΔT_{s2} : the arrival and duration of the shear waves induced by shock wave-to-S conversion at the cavity wall (Eq.(3.82))
Ts3_e and Ts3_l: the possible earliest and last arrival of the shear waves induced by macrocracking (Eqs.(3.86) and (3.87))

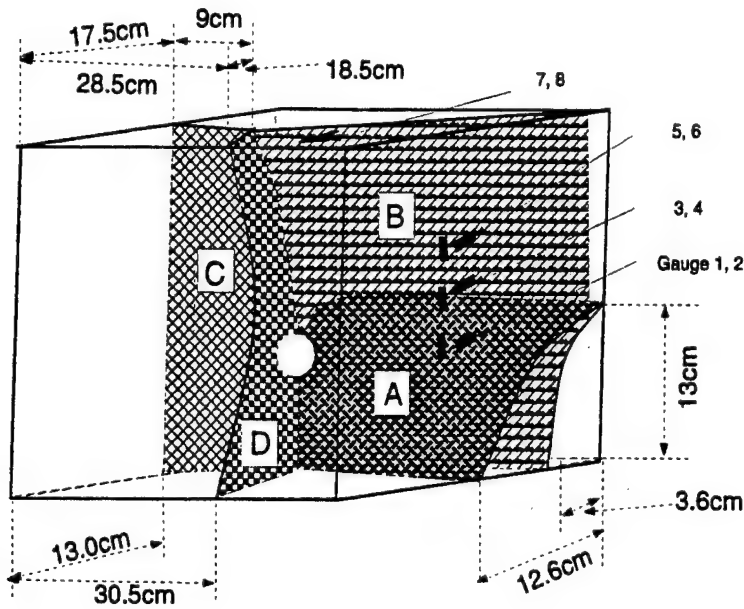


Figure 3.9: Schematic of the large cracks in relation to the spherical cavity.

3.3 Analysis of the P-waves Induced by Explosions and Cracking

3.3.1 P-wave velocity

From the experimental records, the P-wave velocity is determined to be 4.22 km/s under the experimental conditions as shown in figure 3.10 (the data from SW9 was not used because of the noise at the beginning of the signals). The P-wave velocity determined here is somewhat lower than 4.9 km/s measured ultrasonically by Rubin and Ahrens (1991) on a different sample. However, this velocity is still much higher than the bulk velocity (3.68 km/s). This means that the deformation induced by the P-wave is still in the elastic deformation regime over most of its propagation path. The lower P-wave velocity could also be the result of the nonlinear elastic behavior of the rock because elastic wave velocity decreases with amplitude in rocks.

3.3.2 Particle displacement induced by P-waves

Using the relations between strains and displacements given in Chapter 2, the P-wave particle displacements are calculated and shown in figure 3.11 for SW4 and figure 3.12

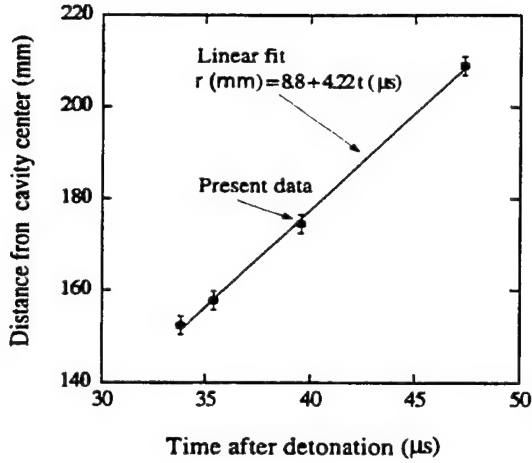


Figure 3.10: P-wave arrival versus radius.

for SW9. From figures 3.11 and 3.12, the maximum P-wave particle displacements, u_{max} , at different distances from the cavity center can be obtained and are shown in figure 3.13 in which Cowboy data (Murphrey, 1961) are plotted. The experimental data is fit by

$$u_{max} = 1.32 \times 10^4 r^{-1.46}, \quad \text{for SW4} \quad (3.2)$$

$$u_{max} = 1.93 \times 10^4 r^{-1.56}, \quad \text{for SW9} \quad (3.3)$$

where u_{max} is in μm , r in mm is the distance from the cavity center. In Murphrey's(1961) paper, he found that the field results have a dependence of the peak P-wave particle displacement on the distance from the cavity center that is proportional to $r^{-1.5}$. Thus, the previous study is very comparable with the results from this work.

3.3.3 Comparison between experimental data and theoretical predictions

Displacement induced by pulse-spherical waves

The analytic solution for a pulsed spherical wave generated from an explosion in a spherical cavity (Timoshenk and Goodier, 1970) is obtained by solving

$$\frac{\partial \sigma}{\partial r} + \frac{2}{r}(\sigma_r - \sigma_\theta) = \rho \left(\frac{\partial V}{\partial t} + V \frac{\partial V}{\partial r} \right), \quad (3.4)$$

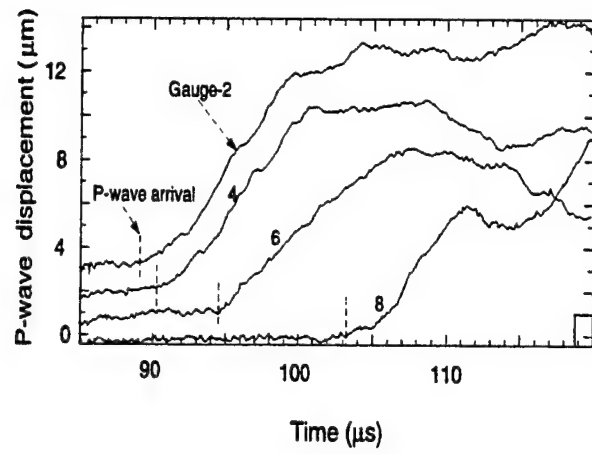


Figure 3.11: P-wave particle displacement versus time for SW4.

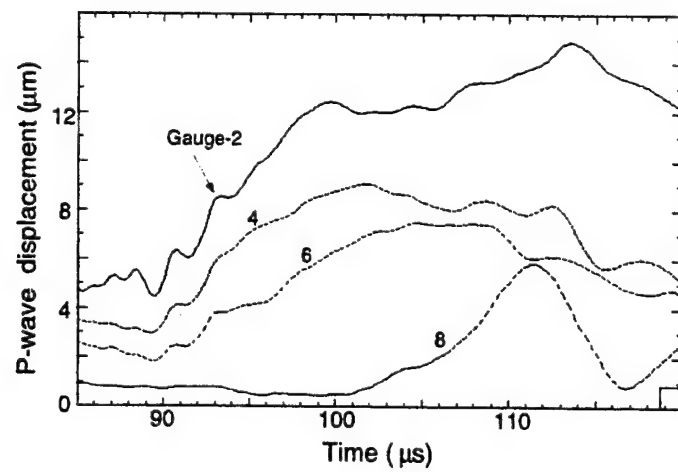


Figure 3.12: P-wave particle displacement versus time for SW9.

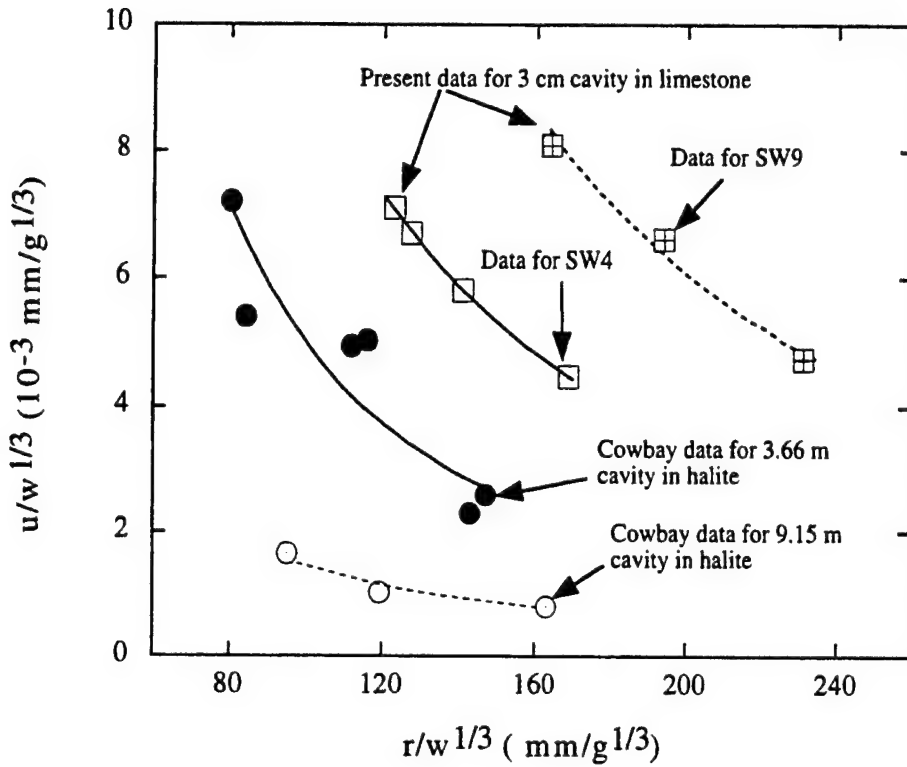


Figure 3.13: Scaled maximum P-wave particle displacement versus propagation distance

u — peak P-wave particle displacement in mm

w — mass of explosives in gram

r — distance from the center of cavity in mm

For Cowboy experiments,

$u/w^{1/3} = 0.55 (r/w^{1/3})^{-1.29}$ for 9.15 meter cavities in which the mass of the explosives detonated ranged from 200 to 1000 lbs,

$u/w^{1/3} = 7.7 (r/w^{1/3})^{-1.59}$ for 3.66 meter cavities in which the mass of the explosives detonated was from 20 to 900 lbs.

For present data,

$$u/w^{1/3} = 7.8 (r/w^{1/3})^{-1.46} \text{ for SW4}$$

$$u/w^{1/3} = 23.4 (r/w^{1/3})^{-1.56} \text{ for SW9}$$

$$\frac{\partial \rho}{\partial t} + \frac{1}{r^2} \frac{\partial(\rho r^2 V)}{\partial r} = 0, \quad (3.5)$$

where ρ is density, V is particle velocity, r is the distance from center of the source.

After using Hooke's law, the wave equation is

$$\frac{\partial^2 u}{\partial r^2} + \frac{2}{r} \frac{\partial u}{\partial r} - \frac{2u}{r^2} = \frac{1}{C_e^2} \frac{\partial^2 u}{\partial t^2}, \quad (3.6)$$

where u is particle displacement and C_e is P-wave velocity.

If pressure at the cavity boundary, $r=a$, is $p(t)$, the displacement (Timoshenk and Goodier, 1970) can be calculated using

$$u = \frac{f'}{C_e r} + \frac{f}{r^2}, \quad (3.7)$$

where f is the solution of

$$f''(t) + 2\gamma f'(t) + \frac{2\gamma C_e}{a} f(t) = \frac{ap(t)}{\rho}, \quad (3.8)$$

where γ is

$$\gamma = \frac{1-2\nu}{1-\nu} \frac{C_e}{a}, \quad (3.9)$$

where ν is Possion's ratio.

The particular solution of Eq.(3.8) for an outgoing wave from a spherical source (Timoshenk and Goodier, 1970) is

$$f(t) = \frac{1}{\alpha - \beta} \frac{a}{\rho} \int_0^t p(\tau) (e^{\alpha_0(t-\tau)} - e^{\beta_0(t-\tau)}) d\tau, \quad (3.10)$$

where

$$\alpha_0 = \gamma(-1 + is), \quad (3.11)$$

$$\beta_0 = \gamma(-1 - is), \quad (3.12)$$

and $s=(1-2\nu)^{-0.5}$.

If a step-like pressure history, i.e., $p(t)=p_0 H(t)$, is assumed, the particular solution

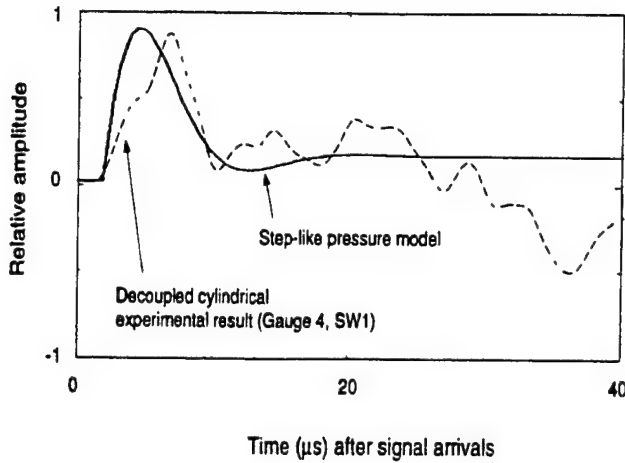


Figure 3.14: Typical displacement history from the spherical model without cracking

(Timoshenkov and Goodier, 1970) is

$$f(\tau) = \frac{p_0 a^2}{2\rho\gamma C_e} \left(1 - e^{\gamma\tau} \left(\cos(\gamma s\tau) + \frac{\sin(\gamma s\tau)}{s} \right) \right), \quad (3.13)$$

where $\tau = t - (r - a)/C_e$.

The displacement history at r (Timoshenkov and Goodier, 1970) is

$$u(t, r) = \frac{A}{r^2} + \frac{A}{C_e} \frac{e^{-\gamma\tau}}{r} \left(\left(\gamma s + \frac{\gamma}{s} - \frac{C_e}{rs} \right) \sin(\gamma s\tau) - \frac{C_e \cos(\gamma s\tau)}{r} \right), \quad (3.14)$$

where $A = p_0 a^2 / (2\rho\gamma C_e)$.

The first term in the solution corresponds to the static solution, the second is dynamic term. The typical displacement history from Eq.(3.14) is shown in figure 3.14 in which the experimental data from Shot SW1 also is shown (see Chapter 4). From this figure, we can see that the solution from only pure pulse spherical wave propagation can explain the P-wave profile from the experiments without cracking but not explain the observed results as shown in figures 3.11 and 3.12.

The reasons for the difference may include:

1. The pressure history in cavity is not a single-step-like function. Because of the large mismatch of impedances between gas in cavity and rocks, shock waves generated by explosions in cavity generally reverberate several times before the pressure in cavity reaches its final value. This means that the pressure history in

- cavity may have a multi-step history. This also can be seen from the experimental data as shown in figure 3.11 and 3.12;
2. The cracking processes may play a very important role in the P-wave induced displacement history because radial cracking generated by the pressure in cavity and P-wave propagation changes the boundary conditions for the field. When pressure in cavities is larger than some critical value, radial cracks are generated from inner surfaces. The radial cracks will make the tangential stress be either zero if the explosion products do not penetrate into cracks or the same pressure as in the cavity if the explosion products do penetrate into cracks. Whenever the explosion products penetrate into cracks or not, the tangential stress in rocks has a large jump during cracking because the tangential stress is tensional before cracking and compressional after cracking. These rapid changes give rise to shear waves. Radial cracking also generates P-waves because cracking is equivalent to increase cavity radius (a crack opening does not apparently change the pressure in cavity).

Displacement induced by the P-waves generated from explosions and cracking

Basing on the analysis above, we construct a model considering the reverberation of shock waves in cavity and the P-waves generated from radial cracking process.

1. Pressure history

In this model, we assume that the pressure history is divided into three time periods, i.e. reverberation dominated period, cracking dominated period and steady period. The pressure history acted on the cavity wall can be given by

$$p(t) = p_I(t)(H(t) - H(t - t_0)) + p_{II}(t)(H(t - t_0) - H(t - t_{00})) + p_{III}H(t - t_{00}), \quad (3.15)$$

where $p_I(t)$, $p_{II}(t)$ and $p_{III}(t)$ are the pressure histories that correspond to the three periods, respectively. $H(t)$ is step function. t_0 and t_{00} are the start and stop time of crack propagation. The pressure history for each period in cavities is estimated approximately as

(I) Reverberation dominated period:

Shock waves induced by detonation of an explosive reverberate in a cavity, the pressure acted on cavity wall is multi-step and radial cracks have not yet propagated in rock.

During this period, it is assumed that the pressure acted on the wall of cavity between two adjacent reverberations is constant, we have

$$p_I(t) = \sum_{i=1}^N p_i H(t - t_i), \quad (3.16)$$

where p_i is pressure increment after each reflection, t_i is the reflection time for i th step and N is reverberation times.

(II) Cracking dominated period:

In general, there are two kinds of cracks induced by the explosions in cavity. The first is the nucleation of new cracks and growth of existing cracks (micro-cracks) related to P-wave propagation, the second type of cracks is the macro-cracks that start from the cavity wall and propagate into rock. Micro-cracks appears just after P-wave if stress related with P-wave is higher than the local tensional strength. Macro-crack propagation is controlled by fracture dynamics. In this part, only the P-wave generated from macro-cracking is considered because P-waves generated from micro-cracks can not be separated from the initial P-waves and also have small amplitude.

When pressure in cavities is larger than some critical value, radial cracks are generated from inner surfaces. The tangential stress in rocks has a large change during cracking because the tangential stress is tensional before cracking and compressional after cracking. Radial cracking generates P-waves because cracking is equivalent to increase pressure in a cavity.

There are two ways to approximately estimate the effect of cracking on displacements.

(a) The first is to solve the differential equation with moving boundary as

$$f''(t) + 2\gamma(t)f'(t) + \frac{2\gamma(t)C_e}{a(t)}f(t) = \frac{a^r(t)p(t)}{\rho}, \quad (3.17)$$

where

$$\gamma(t) = \frac{1-2\nu}{1-\nu} \frac{C_e}{a^r(t)}, \quad (3.18)$$

and

$$a^r(t) = a + \int_{t_0}^t C^c(\tau)d\tau, \quad (3.19)$$

where $a^r(t)$ is radius of the crack tip to the center of the cavity, t_0 is the time at which cracks start to propagate, C^c is crack propagation velocity. Numerical solution may be applicable to Eq.(3.17) but the moving boundary with fracture is also very difficult to deal with.

(b) To obtain an approximate pressure profile, we assume that the pressure in a cavity changes basing on that the total force acted on the spherical surface with radius $a^r(t)$ is equal to the force acted on the surface with radius a ,

$$p(t)a^2 = p_0(a + \int_{t_0}^t C^c d\tau)^2, \quad (3.20)$$

where p_0 is the pressure in cavity just before cracks start to propagate and we assume that the radial stress at the spherical surface with radius $a^r(t)$ is equal to p_0 . This gives the equivalent pressure in cavity as

$$p(t) = p_0(1 + \int_{t_0}^t \frac{C^c}{a} d\tau)^2, \quad t \geq t_0, \quad (3.21)$$

(III) Steady period:

After cracking stops, the pressure in cavity is assumed to be constant

$$p_{III} = p_{II}(t_{00}). \quad (3.22)$$

2. Solutions for the three periods

(a) Solution for period I

From Eq.(3.14), the displacement induced by i th reverberation at r is

$$u_i(\tau_i, r) = \frac{A_i}{r^2} + A_i \frac{e^{-\gamma\tau_i}}{rC_e} \left((\gamma s + \frac{\gamma}{s} - \frac{C_e}{rs}) \sin(\gamma s \tau_i) - \frac{C_e \cos(\gamma s \tau_i)}{r} \right), \quad (3.23)$$

where $A_i = p_i a^2 / (2\rho\gamma C_e)$, $\tau_i = t - t_i - (r - a)/C_e$ and t_i is the i th reverberation time.

the resultant solution is just the superposition of the solutions for all N reverberations. The displacement field induced by reverberations at r is

$$u^I = \sum_{i=1}^N u_i H(t - t_i). \quad (3.24)$$

(b) Solution for period II

In order to obtain an analytic expression, the crack velocity is assumed to be the two simplest cases as:

- (1) Case a: crack velocity remains constant during crack propagation.
- (2) Case b: crack velocity decreases linearly with time, i.e.,

$$C^c(t) = C_0^c \left(1 - \frac{t - t_0}{t_d}\right), \quad (3.25)$$

where t_d is the total cracking duration, C_0^c is the initial crack propagation velocity and t_0 is the time for cracks to start to propagate.

For Case (a), the pressure history in period II is

$$p(t) = p_0 \left(1 + \frac{C_0^c}{a} (t - t_0)\right)^2. \quad (3.26)$$

Substituting Eq.(3.26) into Eq.(3.10), the solution is found to be

$$f(\tau) = X_0 + X_1 \tau + X_2 \tau^2 + X_5 K_1(\tau) + X_6 K_2(\tau), \quad (3.27)$$

where

$$X_0 = A_0 \left(\frac{p_0}{\gamma^2} + \frac{2p_1}{\gamma^3(1+s^2)} + \frac{p_2(3-s^2)}{\gamma^4(1+s^2)^2} \right), \quad (3.28)$$

$$X_1 = A_0 \left(\frac{p_1}{\gamma^2} + \frac{4p_2}{\gamma^2(1+s^2)} \right), \quad (3.29)$$

$$X_2 = \frac{A_0 p_2}{\gamma^2}, \quad (3.30)$$

$$X_5 = A_0 \left(\frac{p_0}{\gamma^2} - \frac{2p_1}{\gamma^3(1+s^2)} + \frac{2p_2(s^2-3)}{\gamma^4(1+s^2)^2} \right), \quad (3.31)$$

$$X_6 = A_0 \left(-\frac{p_0}{\gamma^2 s} + \frac{p_1(s^1-1)}{\gamma^3 s(1+s^2)} + \frac{2p_2(3s-s^{-1})}{\gamma^4(1+s^2)^2} \right), \quad (3.32)$$

$$A_0 = \frac{a}{\rho(1+s^2)}, \quad (3.33)$$

$$K_1 = e^{-\gamma\tau} \cos(\gamma s\tau), \quad (3.34)$$

$$K_2 = e^{-\gamma\tau} \sin(\gamma s\tau), \quad (3.35)$$

$$p_1 = 2p_0 \frac{C_0^c}{a}, \quad (3.36)$$

$$p_2 = p_0 \left(\frac{C_0^c}{a} \right)^2 \quad (3.37)$$

and

$$\tau = t - \frac{r-a}{C_e} - t_0. \quad (3.38)$$

Substituting Eq.(3.27) into Eq.(3.7), the displacement history in period II is

$$\begin{aligned} u^{II}(\tau) = & \left(\frac{X_1}{C_e r} + \frac{X_0}{r^2} \right) + \left(\frac{2X_2}{C_e r} + \frac{X_1}{r^2} \right) \tau + \frac{X_2}{r^2} \tau^2 + \\ & + \left(\frac{\gamma s X_6 - \gamma X_5}{C_e r} + \frac{X_5}{r^2} \right) K_1 + \left(\frac{X_6}{r^2} - \frac{\gamma X_6 + \gamma s X_5}{C_e r} \right) K_2. \end{aligned} \quad (3.39)$$

For Case b, the pressure history is

$$p = p_0 \left(1 + \frac{C_0^c}{a} \left((t-t_0) - \frac{(t-t_0)^2}{2t_d} \right) \right)^2. \quad (3.40)$$

Substituting Eq.(3.40) into Eq.(3.10), the solution is

$$f(\tau) = a_0 + a_1 \tau + a_2 \tau^2 + a_3 \tau^3 + a_4 \tau^4 + a_5 K_1 + a_6 K_2, \quad (3.41)$$

where

$$\begin{aligned} a_0 &= A_0(b_1 p_0 + 2p_1 b_2 + p_2 b_3(3 - s^2) + 24p_3 b_4(1 - s^2) + \\ &\quad + 24p_4 b_5(1 - 6s^2 + s^4 + 4s - 4s^3)s^{-1}), \end{aligned} \quad (3.42)$$

$$a_1 = A_0(p_1 b_1 + 4p_2 b_2 + 6b_3(3 - s^2) + 96p_4 b_4(1 - s^2)), \quad (3.43)$$

$$a_2 = A_0(p_2 b_1 + 6p_3 b_2 + 12p_4 b_3(3 - s^2)), \quad (3.44)$$

$$a_3 = A_0(p_3 b_1 + 8p_4 b_2), \quad (3.45)$$

$$a_4 = A_0 p_4 b_1, \quad (3.46)$$

$$\begin{aligned} a_5 &= A_0(-b_1 p_0 + -2p_1 b_2 + 2(s^2 - 3)p_2 b_3 - \\ &\quad 24p_3(1 - s^2)b_4 - 24p_4(1 - 6s^2 - 4s^3 + s^4 + 4s)b_5 s^{-1}), \end{aligned} \quad (3.47)$$

and

$$\begin{aligned} a_6 &= A_0(-b_1 p_0 s^{-1} b_2 p_1(s^2 - 1)s^{-1} + 2b_3 p_2(3s - s^{-1}) - 6b_4 p_3(s^{-1} - 6s + s^3) - \\ &\quad - 24b_5 s^{-1} p_4((1 + s^2)^5 - (1 + 4s - 6s^2 - 4s^3 + s^4)^2)^{0.5}), \end{aligned} \quad (3.48)$$

where

$$b_1 = \frac{1}{\gamma^2}, \quad (3.49)$$

$$b_2 = \frac{1}{\gamma^3(1 + s^2)}, \quad (3.50)$$

$$b_3 = \frac{1}{\gamma^4(1+s^2)^2}, \quad (3.51)$$

$$b_4 = \frac{1}{\gamma^5(1+s^2)^3}, \quad (3.52)$$

$$b_5 = \frac{1}{\gamma^6(1+s^2)^4}. \quad (3.53)$$

$$p_1 = \frac{2c_0^c p_0}{a}, \quad (3.54)$$

$$p_2 = p_0 \left(\left(\frac{C_0^c}{a} \right)^2 - \frac{C_0^c}{at_d} \right), \quad (3.55)$$

$$p_3 = -\frac{C_0^2 p_0}{a^2 t_d}, \quad (3.56)$$

$$p_4 = \frac{p_0}{4} \left(\frac{C_0^c}{at_d} \right)^2, \quad (3.57)$$

Substituting Eq.(3.41) into Eq.(3.7), the displacement history in period II for Case b is

$$\begin{aligned} u^{II}(\tau) = & \left(\frac{a_1}{C_e r} + \frac{a_0}{r^2} \right) + \left(\frac{2a_2}{C_e r} + \frac{a_1}{r^2} \right) \tau + \left(\frac{a_2}{r^2} + \frac{3a_3}{C_e r} \right) \tau^2 + \left(\frac{4a_4}{C_e r} + \frac{a_3}{r^2} \right) \tau^3 + \\ & + \frac{a_4}{r^2} \tau^4 + \left(\frac{\gamma s a_6 - \gamma a_5}{C_e r} + \frac{a_5}{r^2} \right) K_1 + \left(\frac{a_6}{r^2} - \frac{\gamma a_6 + \gamma s a_5}{C_e r} \right) K_2. \end{aligned} \quad (3.58)$$

(c) Solution for period III

Substituting Eq.(3.22) into Eq.(3.10), the solution is

$$f(t) = \frac{p_1 a^2}{2\rho\gamma C_e} \left(1 - e^{-\gamma t} \left(\cos(\gamma s t) - \frac{\sin(\gamma s t)}{s} \right) \right), \quad (3.59)$$

then, substituting Eq.(3.59) into Eq.(3.7), the displacement is

$$u^{III}(\tau) = \frac{p_1 a^2}{2\rho\gamma C_e r} \left(\frac{C_e}{r} + e^{-\gamma\tau'} \left(\left(\frac{\gamma}{s} + \gamma s - \frac{C_e}{rs} \right) \sin(\gamma s \tau') - \frac{C_e \cos(\gamma s \tau')}{r} \right) \right). \quad (3.60)$$

where

$$\tau' = \tau + t_{III}. \quad (3.61)$$

3. Displacement history induced by P-waves

Then the displacement history induced by P-waves is

$$u = u^I(H(\tau) - H(\tau - t_0)) + u^{II}(H(\tau - t_0) - H(\tau - t_{00})) + u^{III}H(\tau - t_{00}), \quad (3.62)$$

3.3.4 Comparison between the observation and theoretical predictions of displacement history induced by P-waves

Parameters estimation

Because the ratio of cavity radius to explosive radius is about 3, there is no separation between shock wave in air in the cavity and the adiabatic release wave of explosion products. The shock wave velocity in air can be estimated using CJ theory. The particle velocity after the CJ detonation is

$$V_p = \frac{D}{\gamma + 1}, \quad (3.63)$$

where D is CJ wave velocity.

For PETN, the typical CJ wave velocity is 8 km/s (Dobratz, 1974). The particle velocity then is about 3.3 km/s. The vibration period in the cavity is

$$t_v \approx a / (2 * 3.3) \approx 2.3 \mu s. \quad (3.64)$$

From experimental data, the rise-time of the particle displacement induced by P-wave is $\sim 10 \mu s$, about three time vibrations. This also can be verified from the profiles of the displacement rise-front from the experiments. Then, we have N=3, $t_1=0.0$, $t_2=4.6 \mu s$, $t_3=9.2 \mu s$, $p_1=p_2=p_3=p_0/3$. Also, $t_0=10.0 \mu s$.

It theoretically is found that the maximum velocity of a mode-I crack is Rayleigh

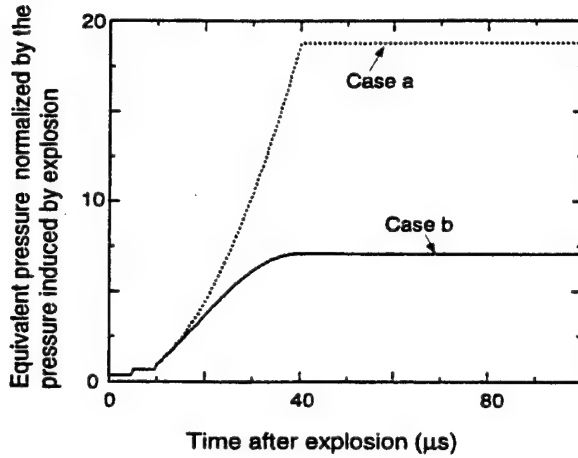


Figure 3.15: Pressure history

wave velocity(Freund and Clifton, 1972). Compared to the crack velocity in rocks from seismology (Hiroo Kanomori, 1993), the fault propagation velocity is $\sim 70\%$ of the theoretical maximum velocity of a mode-II crack, i.e., shear wave velocity. Crack propagation velocity, C^c , is assumed to be 70% of Rayleigh wave velocity, C_R , because the cracks generated in the experiments are mode-I. Then, t_{00} is

$$t_{00} = \frac{L_c}{0.7C_R} + t_0, \quad \text{for Case a} \quad (3.65)$$

$$t_{00} = \frac{2 * L_c}{0.7C_R} + t_0, \quad \text{for Case b} \quad (3.66)$$

where L_c is crack length.

For shot SW4, the crack length with the explosion product trace on it is roughly about 50 mm, so $t_{00} \approx 38 \mu s$ for Case a and $65 \mu s$ for Case b.

Pressure history in cavity

Based on the parameters estimated above, the pressure profiles normalized by p_0 for Shot SW4 are schematically shown in figure 3.14.

Displacement history

Figure 3.15 shows the calculated results of displacement time history based on the pressure history Case a and Case b. From this figure, it seems that the displacement

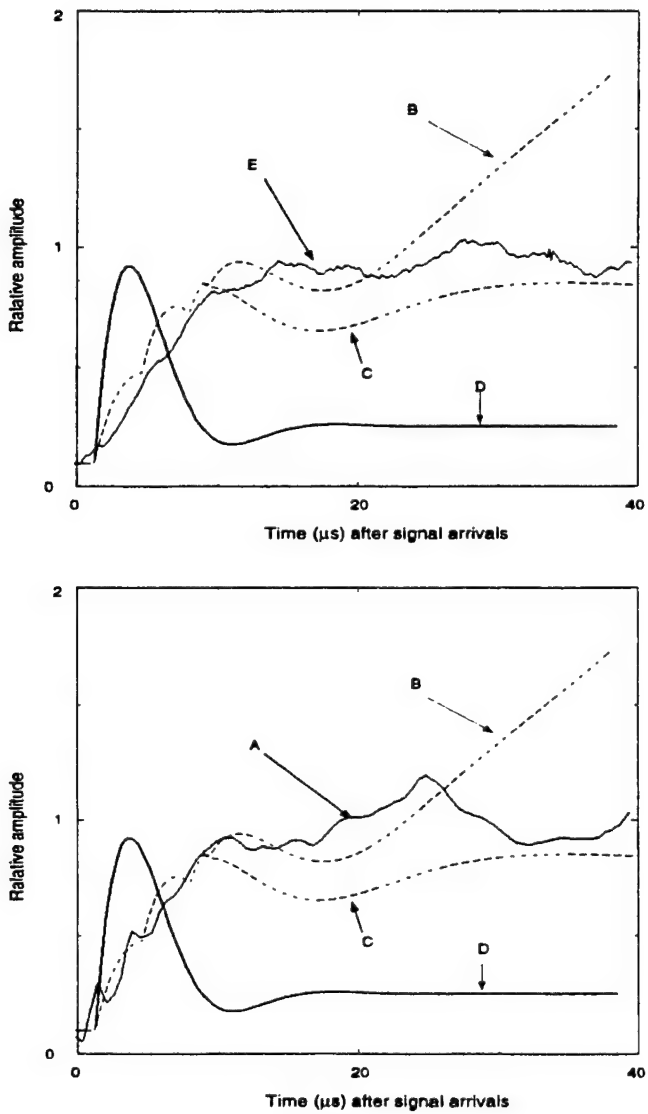


Figure 3.16: Comparison between the experimental data and the results from the equivalent models

- A: Shot SW4, Gauge 2,
- B: Constant crack velocity model (Eqs.(3.24) and (3.39)),
- C: Constant deceleration model (Eqs.(3.24) and (3.58)),
- D: Constant step pressure model (Eq.(3.14)),
- E: Shot SW9, Gauge 4

history recorded from experiments is between the two extreme conditions, that may reflect the real situation that cracks propagate neither at constant velocity nor at constant deceleration. From the comparison between the theoretical estimation based on Cases a and b and the experimental data, cracking process has very large effect on the history of displacement or strain. First, cracking processes increase the amplitude of low frequency component because cracking is equivalent to increase the pressure duration in a cavity. Second, cracking processes increases the complexity of the directional dependence of displacement history because of nonuniform distribution of cracks.

3.3.5 P-wave decay

From the solutions from the model we constructed for Period I as given in Eq.(3.24), the peak displacement at r induced by P-wave is

$$u_{max} = \frac{A_1}{r^2} + \frac{B_1}{r}, \quad (3.67)$$

where

$$A_1 = \frac{a^2}{2\rho\gamma C_e} \sum_i^N p_i (1 - \exp(-\gamma\tau_i)) \left(\frac{\sin(\gamma s\tau_i)}{s} + \cos(\gamma s\tau_i) \right), \quad (3.68)$$

and

$$B_1 = \frac{a^2}{2\rho\gamma C_e^2} \sum_i^N p_i (\gamma s + \frac{\gamma}{s}) \sin(\gamma s\tau_i) \exp(-\gamma\tau_i). \quad (3.69)$$

A_1 and B_1 can be determined experimentally using the measured maximum data at different distance from the source. The best fit to the measured data is shown in figure 3.16. The best fit expressions are

$$u_{max} = 1.005 \times 10^5 r^{-2} + 676.6 r^{-1}, \quad \text{for SW4}, \quad (3.70)$$

$$u_{max} = 0.953 \times 10^5 r^{-2} + 530.1 r^{-1}, \quad \text{for SW9}, \quad (3.71)$$

where u_{max} is in μm and r is in mm.

Based on the relation between maximum P-wave particle displacement and the

propagation distance, the maximum radial strain, ε_r , and tangential strain, ε_t , for SW4 are

$$\varepsilon_r = \frac{\partial u_{max}}{\partial r} = -201r^{-3} - 0.677r^{-2}, \quad (3.72)$$

$$\varepsilon_t = \frac{u_{max}}{r} = 100.5r^{-3} + 0.677r^{-2}. \quad (3.73)$$

and for SW9

$$\varepsilon_r = \frac{\partial u_{max}}{\partial r} = -190.6r^{-3} - 0.53r^{-2}, \quad (3.74)$$

$$\varepsilon_t = \frac{u_{max}}{r} = 95.3r^{-3} + 0.53r^{-2}. \quad (3.75)$$

From Hooke's law, we have

$$\sigma_r = \frac{E}{(1+\nu)(1-2\nu)}((1-\nu)\varepsilon_r + 2\nu\varepsilon_t) \quad (3.76)$$

$$\sigma_t = \frac{E}{(1+\nu)(1-2\nu)}(\varepsilon_t + \nu\varepsilon_r), \quad (3.77)$$

where σ_r and σ_t are radial and tangential stresses, respectively. Here, ν is Poisson's ratio. Based on the experimental data, ν is 0.258 for the limestone and E is 47.7 GPa. We have the maximum stresses,

for SW4:

$$\sigma_r = -1.19 \times 10^4(636r^{-3} + r^{-2}), \quad (3.78)$$

$$\sigma_t = 3.92 \times 10^4(96.8r^{-3} + r^{-2}), \quad (3.79)$$

for SW9:

$$\sigma_r = -0.94 \times 10^4(768r^{-3} + r^{-2}), \quad (3.80)$$

$$\sigma_t = 3.06 \times 10^4(117r^{-3} + r^{-2}), \quad (3.81)$$

3.4 Analysis of the S-waves Generated from Explosions and Cracking

3.4.1 S-wave arrival

Basically, S-waves are generated from at least three different sources:

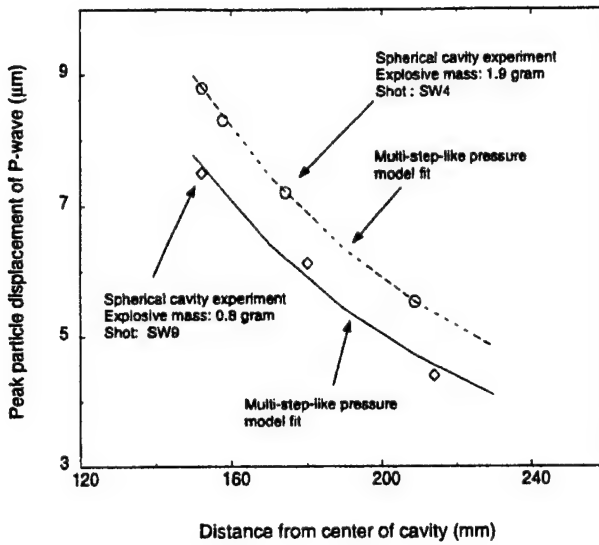


Figure 3.17: Peak P-wave induced particle displacement versus propagation distance

1. Micro-cracking.
2. shock wave-to-S conversion at cavity wall.
3. Macro-cracking.

In the case of each of these three sources, the arrival time of the S-wave from the second source can be estimated with relatively high accuracy because we know the P-wave arrival time at the cavity wall. The arrival time at radial distance, r , of the S-wave from the second source, T_{s2} , is

$$T_{s2} = \frac{C_e - C_s}{C_e C_s} (r - a) + \frac{r - a}{C_e}, \quad (3.82)$$

where, C_s is S-wave velocity.

The duration of the S-wave, ΔT_{s2} , should approximately equate to the rise time of P-waves.

The arrival time at radial distance, r , of the S-wave from the first source is

$$T_{s1} = \frac{C_e - C_s}{C_e C_s} (r - R_c) + \frac{r - a}{C_e}, \quad (3.83)$$

where R_c is the radius beyond which there is no micro-cracks induced by P-waves. The duration of this S-wave, $\Delta Ts1$, is

$$\Delta Ts1 = \frac{C_e - C_s}{C_e C_s} (R_c - a). \quad (3.84)$$

The accuracy of this arrival time is dependent on how to determine R_c (in the following estimation, R_c is chosen to be 50 mm based on the experimental data).

The arrival time, $Ts3$, of the S-wave from the third source is

$$Ts3 = \frac{C_e - C_s}{C_e C_s} (r - a) + t_0 + \frac{(a^2 + r^2 - 2ar \cos(\theta_c))^{1/2} - (r - a)}{C_s}, \quad (3.85)$$

where θ_c is the angle between the two radial lines one of which points to the nearest macro-crack generated and the other points to the gauge location. The last term on the right hand side in Eq. (3.85) is from the fact that the S-wave from the cracks that is not along the line connecting the gauge with the center of the cavity arrives later. The earliest and last arrival times, $Ts3_e$ and $Ts3_l$, are correspond to $\theta_c = 0$ and $\theta_c = 90^\circ$, respectively. Then, we have,

$$Ts3_e = \frac{C_e - C_s}{C_e C_s} (r - a) + t_0, \quad (3.86)$$

$$Ts3_l = \frac{C_e - C_s}{C_e C_s} (r - a) + t_0 + \frac{(a^2 + r^2)^{1/2} - (r - a)}{C_s}. \quad (3.87)$$

Using the expressions above, the three S-wave arrivals are marked on the records shown in figures 3.7 and 3.8. From these figures, the predictions are in very good agreements with the experiment data for $Ts2$ and $Ts3$. The data clearly demonstrates the S-wave generated from shock wave-to-S conversion on cavity wall and cracking.

3.4.2 S-wave amplitudes

Figure 3.18 shows the maximum strains from the gauges along direction 2 (Fig. 2.1) for shear waves generated from shock wave-to-S conversion and macro-cracking at different locations for Shot SW4 and SW9. Due to the difficulty to determine the S-wave incident angle at each gauges directly, the two gauges at the same location is used to determine the incident angle approximately and then the peak displacement

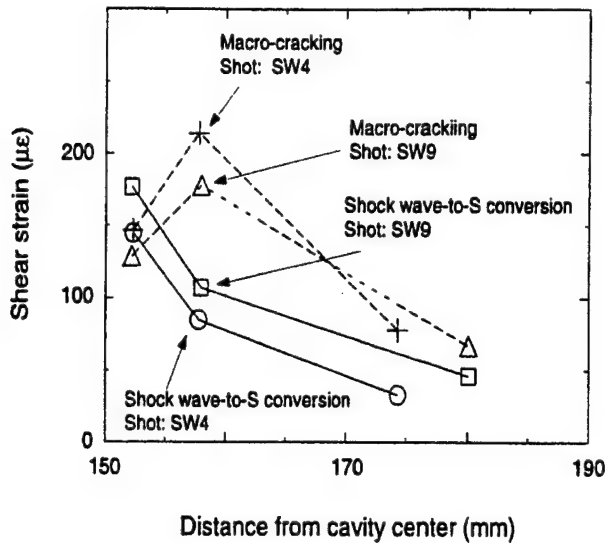


Figure 3.18: Maximum shear wave strain versus propagation distance

of the S-waves are determined. The procedure to determine S-wave incident angle using the two gauges at the same location is: (1) to find out the ratio of the strain from the gauge along direction 2 to the strain from the gauge along direction 1; (2) to calculate the incident angle using the ratio and Eqs.(2.42) and (2.40). We must mention that this method is not very precise because P-waves interfere with S-waves but at least it gives the first-order estimate of S-wave amplitudes induced by shock wave-to-S conversion at cavity wall and crack propagation in rock. Figure 3.19 shows the maximum displacement of S-waves at different distance from source. From this figure, it seems that the shear wave generated from shock wave-to-S conversion has higher regularity than the shear wave generated from macro-cracking regarding the amplitude decay with distance, this just clearly shows the complexity of shear waves due to crack propagation. The increase of the S-wave amplitude generated by shock wave-to-S conversion at cavity wall is believed to be from the source.

3.4.3 S-wave profiles generated from cracking

The S-wave amplitudes and profiles recorded by different gauges are dependent on the relative orientation of the gauges with respect to specific cracks (similar, in some respects, to the directivity of wave profile in seismology). It is not surprised to

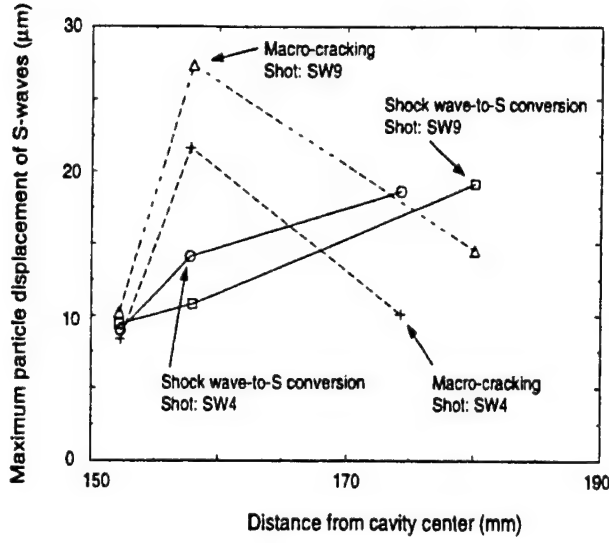


Figure 3.19: Maximum shear wave displacement versus propagation distance

see that the S-wave profiles generated from cracking vary so much from gauge to gauge. In order to calculate S-wave profiles generated by cracking, we assume that the shear strain decays with radial distance following the same rule as P-waves does(this assumption results in lower estimation of S-wave amplitude because P-wave generally decays much faster than S-wave does(Lay and Wallace, 1995) but does not have effects on the wave profiles, and we only consider the wave profile here), then

$$\varepsilon_s = \sum_i \varepsilon_{s,i}^0 \left(\frac{a_{ci}(t)}{r} \right)^{2.5}, \quad (3.88)$$

where $\varepsilon_{s,i}^0$ is the shear strain increase generated from the i th crack extending to radius $a_{ci}(t)$, ε_s is the shear strain observed at r .

In order to obtain an order-of-magnitude estimate of shear waves profiles generated from cracks, we assume that resultant shear strain from multi-cracks is equivalent to that from a single crack that propagates toward to gauges. Then, the shear strain profile is estimated assuming an equivalent crack propagation velocity. We still only consider the two extreme cases, i.e., crack propagation at constant velocity and at constant deceleration.

For constant velocity model, the shear strain profile will be

$$\varepsilon_s = \varepsilon_{si}^0 ((a + C_0^c(t - t_0))/r)^{2.5}. \quad (3.89)$$

where C_0^c is crack propagation velocity, a is the initial cavity radius and t_0 is the initiation time of cracks.

For constant deceleration model, the shear strain history is

$$\varepsilon_s = \varepsilon_{si}^0 ((a + C_0^c(t - t_0) \frac{t_d + t_0 - t}{t_d})/r)^{2.5}. \quad (3.90)$$

where t_d is time duration of crack propagation.

Based on the two equations above, the shear strain history is calculated as shown in figure 3.20 assuming that crack propagation time is same for both model in order to compare them together. In this figure, it shows that experimental results from gauge 3 for SW4 and SW9 and also the results from the model with the first half part at constant velocity and the second half part at constant deceleration. It seems that a constant deceleration or a constant velocity followed by a constant deceleration fits the data better than the constant velocity.

3.5 Conclusions

Basing the experimental results and the analysis above, we concluded

1. A device is developed to drill spherical cavity with the diameter up to 10 centimeters in rocks.
2. The records from the experiments clearly demonstrate the P-waves generated from both explosions and crack propagation. The peak particle displacement induced by P-waves ranges from 9 to 5 μm at 150 to 210 mm from source for the spherical cavity experiment with 1.9 gram explosives, and 8 to 4 μm at 150 to 220 mm from source for spherical experiment with 0.8 gram explosives. The step-like pressure model can be used to explain the experimental results on the peak P-wave induced particle displacement versus propagation distance from the explosions in spherical cavities.

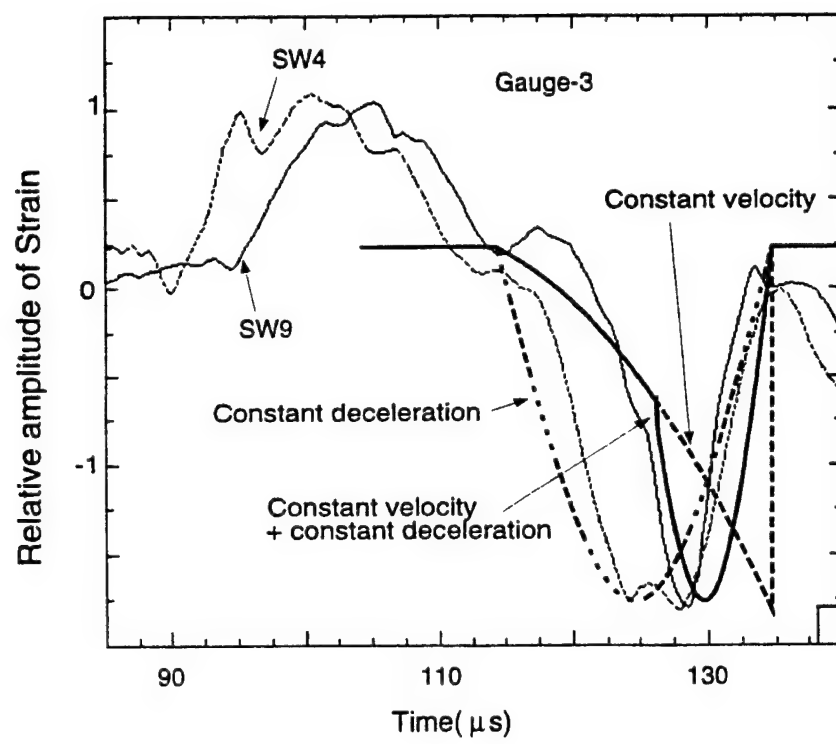


Figure 3.20: Shear strain history

3. More important, the experimental results from the explosions in spherical cavities verify the S-waves generated from both shock wave-to-S conversion at cavity wall and crack propagation in rocks. The amplitude of S-waves from shock wave-to-S conversion is from 10 to 27 μm at 150 to 180 mm from source for the spherical experiment with 1.9 gram explosives, 8 to 21 μm at 150 to 180 mm from source for the spherical experiment with 0.8 gram explosives. The amplitude of S-waves generated by crack propagation is from 9 to 19 μm at 150 to 180 mm from source for the spherical experiment with 1.9 gram explosives, 8 to 19 μm at 150 to 180 mm from source for the spherical experiment with 0.8 gram explosives. The ratio of S-wave to P-wave amplitudes is about 2.
4. A theoretical model including multi-reverberation and crack propagation is proposed to explain the differences on P-wave induced displacement history between the observed and the step-like pressure model. The predicated profiles from this model fits the experimental data qualitatively as shown in Fig. 3.16.
5. A simple dynamical tensional strength model is used to estimate the S-wave profile generated from crack propagation in rock. The S-wave profile predicted from this model fits the experimental data quantitatively.

Chapter 4 Wave Generation From Explosions in Cylindrical Cavities in Rock

4.1 Introduction

Initially to test the apparatus constructed and developed in Chapter 1, we conducted two experiments using a simple cylindrical charge detonated in a cylindrical hole centered in the rock sample depicted in figures 3.3 and 4.1. At same time, the cavity geometrical effects on P- and S-waves generated from explosions can be investigated from the experimental data on spherical and cylindrical cavities.

4.2 Experiments and Results

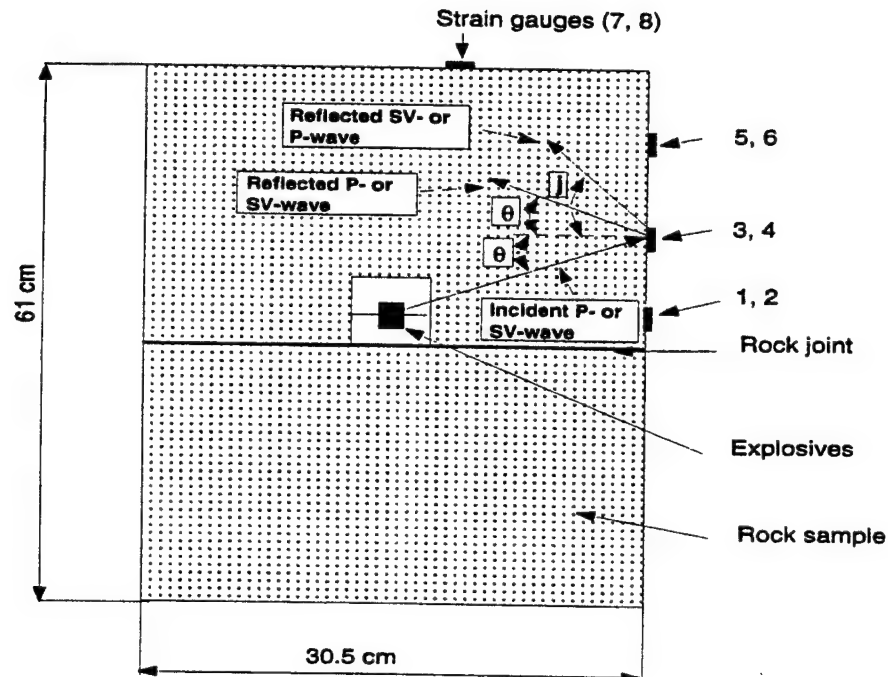
4.2.1 Experimental Details

Two cylindrical test experiments were conducted on Bedford limestone. One was a decoupled explosion, SW1, and the other a tamped explosion, SW2. The parameters used in the experiments and the equilibrium pressure calculated using Eq.(3.1) are listed in Table 4.1.

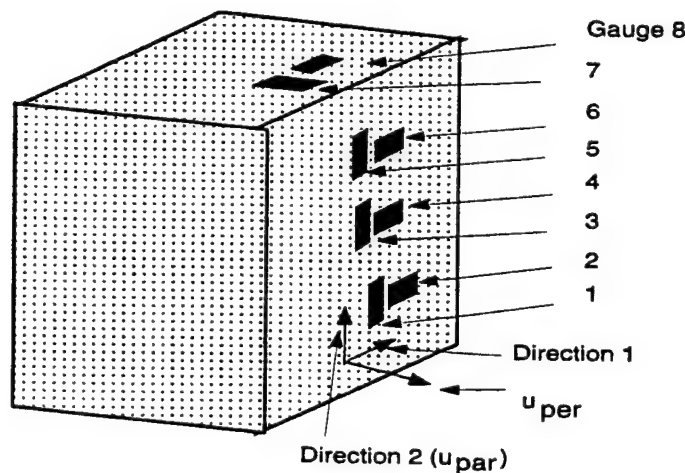
The rock sample is assembled using two blocks as shown in figure 4.1. The rock sample with strain gauges is placed inside a tank pressurized to 10 bar as shown in figure 3.3. To prevent the sample from becoming invaded by water, a plastic film [0.21 mm thickness (Vinyl film sheet No. 8562K5, Warp Bros.)] is wrapped on the surface of the rocks. The gauges and explosives used in experiments are identical to that used in spherical experiments.

4.2.2 Experimental Results

The recorded strains for the two experiments are shown in figures 4.2 for Shot SW1 and figure 4.3 for Shot SW2. From the recovered rock sample, there is minimal damage



(A) Layout of rock sample, strain gauges and explosive charge



(B) Sketch of polarization directions of strain gauges

Figure 4.1: Sample and strain gauge layout for cylindrical cavity experiments

Table 4.1: Data for cylindrical cavity experiments

Shot #		Dimensions of explosives	Mass of explosives	Type of explosives	Dimensions of cavities	p (bar)
SW1	decoupled	$\phi 5 \times 6$ mm	0.24 g	Pellet pressed PETN	$\phi 30 \times 30$ mm	55
SW2	tamped	$\phi 10 \times 10$ mm	1.2 g	Data sheet PETN	$\phi 12 \times 12$ mm	4420

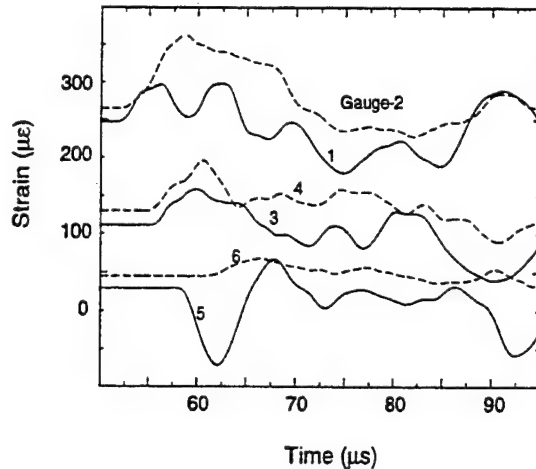


Figure 4.2: Experimental results of the decoupled explosion, Shot SW1
The signals of gauge 7 and 8 are very noisy and are not shown here.

near the cavity wall in the target used for the decoupled experiment, and there are many of the cracks with varying length up to 122 mm and different orientations in the target used for the tamped experiment.

From figure 4.2, it can be seen that the wave profiles from the decoupled experiment, SW1, is very similar to the results from the analytic solution shown in figure 3.13 although the cavity is not spherical. From figure 4.3, the wave profiles from the tamped experiment, SW2, have the typical characteristics of the wave profiles from the spherical experiments. The difference between the decoupled and tamped experiments once again demonstrates the role of cracking in the generation of P- and S-waves because there is minimal damage in the decoupled experiment and the rock sample is heavily cracked in the tamped experiment.

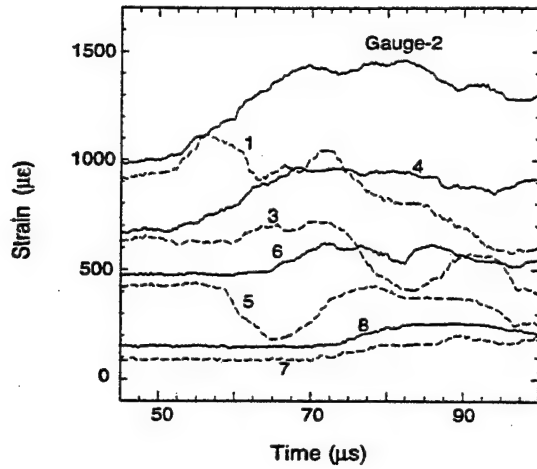


Figure 4.3: Experimental results of the tamped explosion, Shot SW2

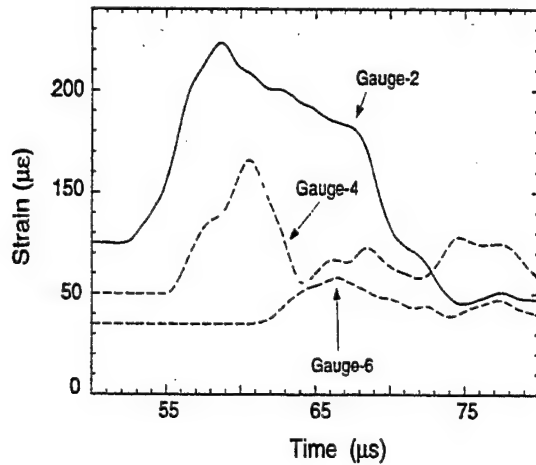


Figure 4.4: P-wave amplitudes from decoupled experiment

4.3 P-waves Generated from Explosions

4.3.1 P-waves generated from the decoupled experiment

Figure 4.4 gives experimental results on the P-wave profiles generated from the decoupled experiment. The peak particle displacements from P-wave are shown in figure 4.6. As mentioned above, although the P-wave profile shape can be explained quantitatively using the analytic solution based on spherical source assumptions as shown in figure 3.13, experimental results show the direction-dependent of the wave shape.

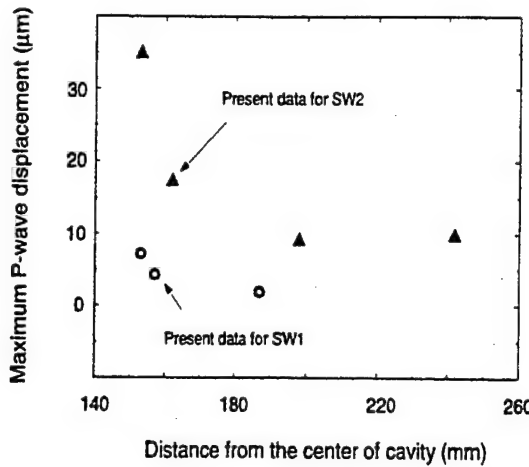


Figure 4.6: P-wave amplitude versus propagation distance for SW1 and SW2

4.4.2 S-waves generated from the tamped experiment

Figure 4.8 gives the arrivals of the three S-waves from the three different source as discussed in section 3.4. As the same as in the spherical experiments, we assume that the macro-cracks start to propagate when P-wave reaches the peak value. The micro-crack radius is chosen to be 122 mm based on the cracks in the recovered target. Although the source is cylindrical, there still is a good agreement between the predicted arrivals of the S-waves and the experimental results. We can see the S-waves from the shock wave-to-S conversion and macrocracks on all the records. Figure 3.9 gives the maximum strain related with the shear waves generated from shock wave-to-S conversion and macrocracking along direction 2.

4.5 Conclusions

From the experimental results of the tamped and decoupled explosions in cylindrical cavities, we concluded

1. The records verified that the characteristics of the signals from the gauges at different locations predicted in Chapter 1. It means that method developed in Chapter 1 can be used to monitor P and S-wave generations from explosions in cavities in rock.

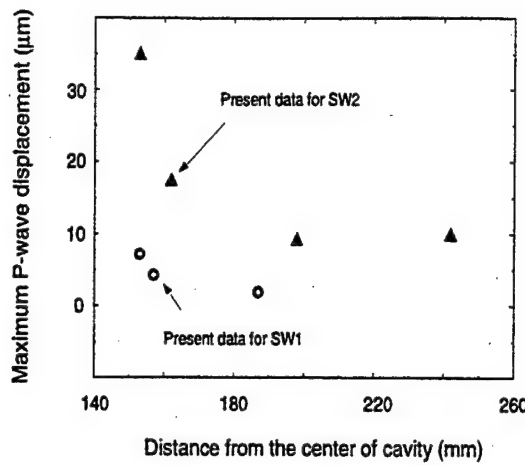


Figure 4.6: P-wave amplitude versus propagation distance for SW1 and SW2

4.4.2 S-waves generated from the tamped experiment

Figure 4.8 gives the arrivals of the three S-waves from the three different source as discussed in section 3.4. As the same as in the spherical experiments, we assume that the macro-cracks start to propagate when P-wave reaches the peak value. The micro-crack radius is chosen to be 122 mm based on the cracks in the recovered target. Although the source is cylindrical, there still is a good agreement between the predicted arrivals of the S-waves and the experimental results. We can see the S-waves from the shock wave-to-S conversion and macrocracks on all the records. Figure 3.9 gives the maximum strain related with the shear waves generated from shock wave-to-S conversion and macrocracking along direction 2.

4.5 Conclusions

From the experimental results of the tamped and decoupled explosions in cylindrical cavities, we concluded

1. The records verified that the characteristics of the signals from the gauges at different locations predicted in Chapter 1. It means that method developed in Chapter 1 can be used to monitor P and S-wave generations from explosions in cavities in rock.

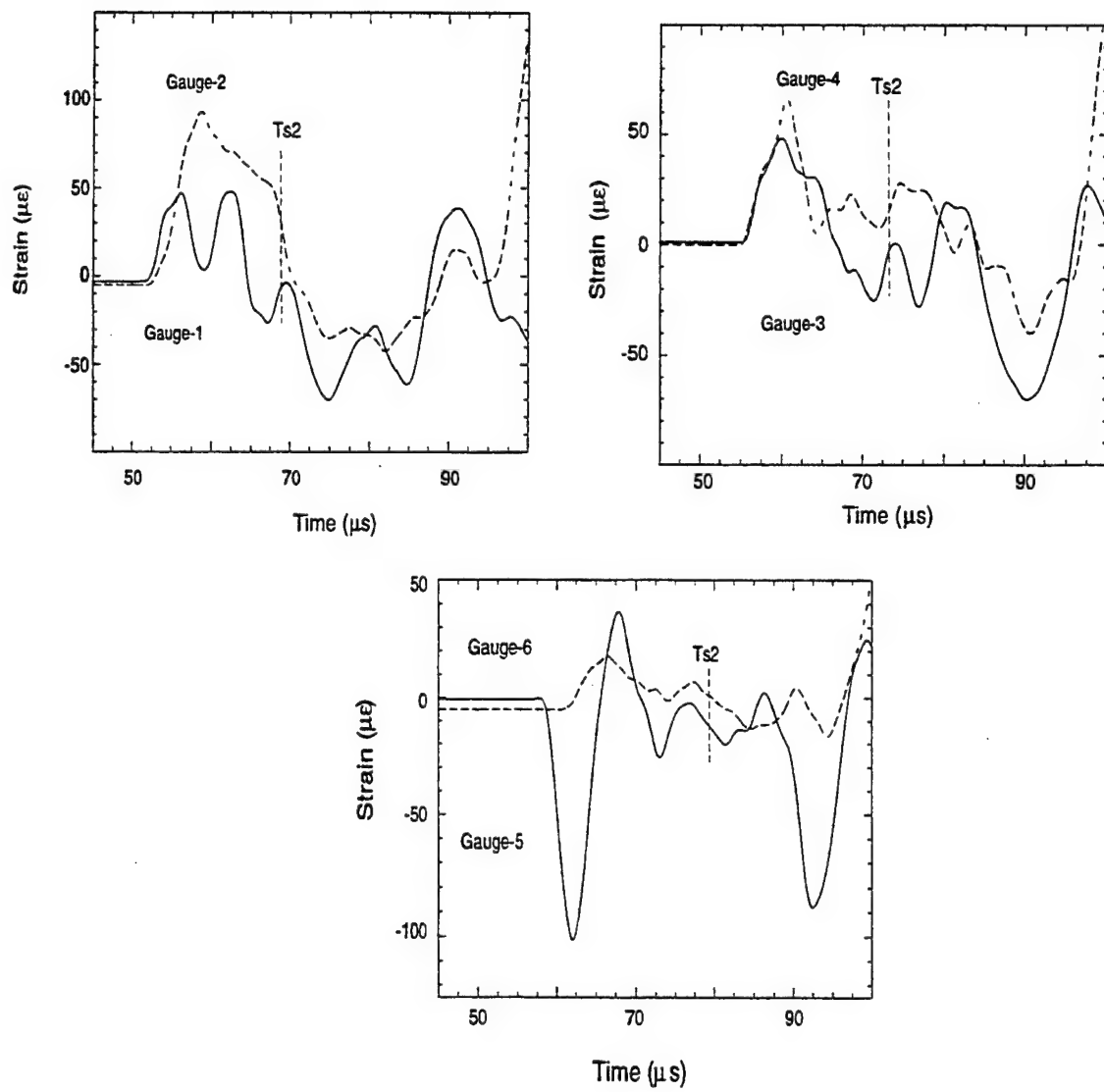


Figure 4.7: Strain signals at different location for SW1

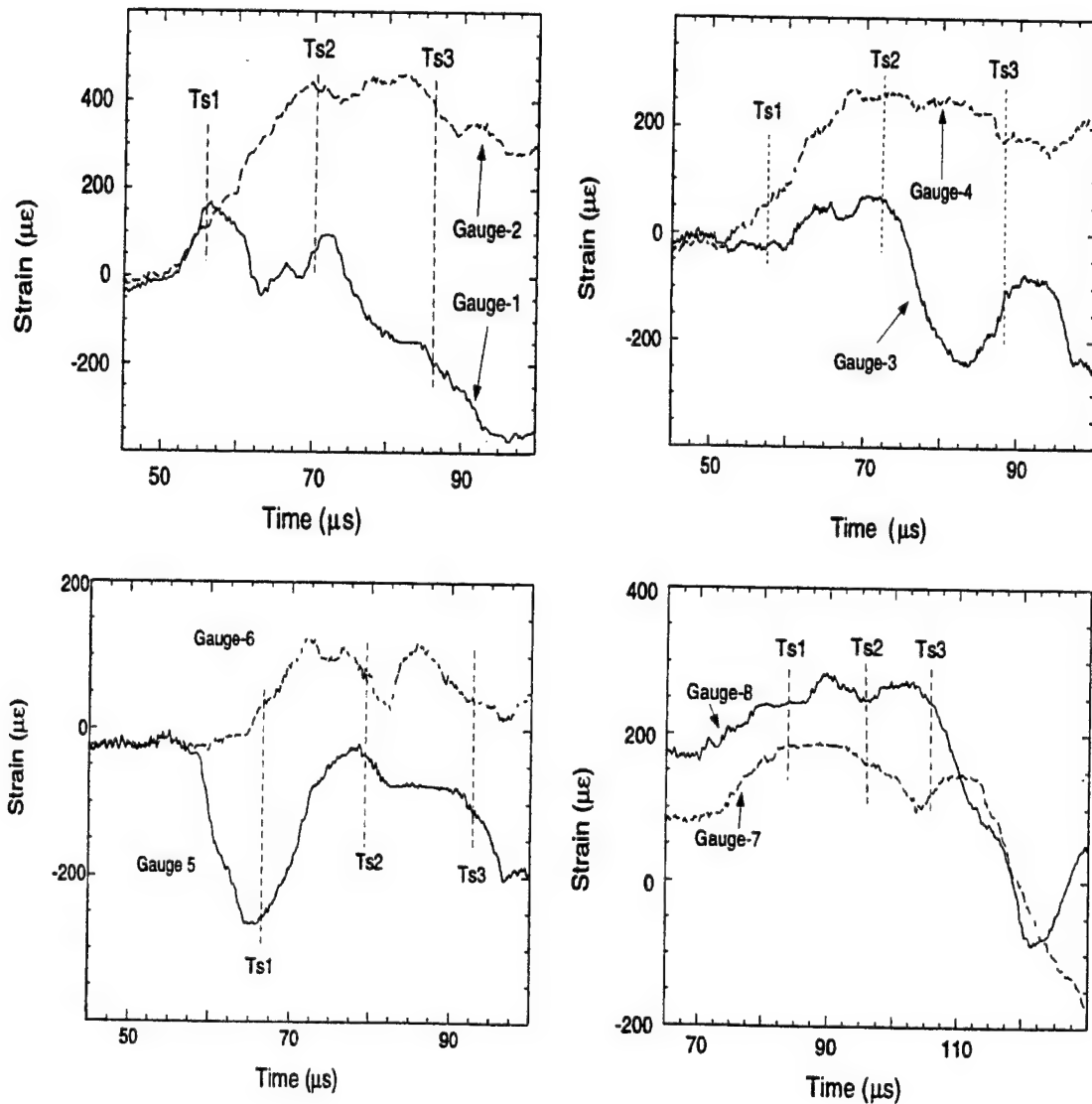


Figure 4.8: Strain signals at the different location for SW2.

- Ts1: the arrival and duration of the shear waves induced by microcracking (Eq.(3.83))
- Ts2: the arrival and duration of the shear waves induced by shock wave-to-S conversion at the cavity wall (Eq.(3.82))
- Ts3: the arrival of the shear waves induced by macocracking (Eq.(3.86))

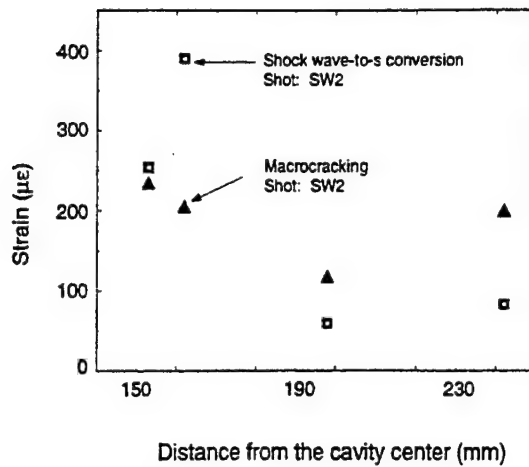


Figure 4.9: S-wave amplitude versus propagation distance for SW1 and SW2

2. The peak particle displacement induced by P-waves ranges from 35 to 10 μm at 150 to 240 mm from source for the tamped cylindrical cavity experiment with 1.2 gram explosives and 7 to 2 μm at 150 to 190 mm from source for the decoupled cylindrical cavity experiment with 0.24 gram explosives. The step-like pressure model can not be used to explain the experimental results on the peak P-wave induced particle displacement versus propagation distance from the explosions in cylindrical cavities. This results demonstrates the cavity geometrical effects on wave pattern.
3. The shear waves generated from shock wave-to-S conversions at cavity wall were observed to be between 50 and 400 $\mu\epsilon$ along direction 2 at 150 to 250 mm from source for tamped explosions. The shear waves induced by crack propagation were recorded to be between 100 and 250 $\mu\epsilon$ along direction 2 at 150 to 250 mm from source for the tamped experiment.

Chapter 5 Summary

Basing on the methods developed and the experimental results and analysis given above, we briefly conclude:

1. A new measuremental method to monitor the P- and S-waves with very high frequency has been developed. The experimental results verify the predicted strain characteristics of P- and S- waves generated from explosions and cracking.
2. A device is developed to drill spherical cavity with the diameter up to 10 centimeters in rocks like limestone.
3. The records from the experiments clearly demonstrate the P-waves generated from both explosions and crack propagation. The peak particle displacement induced by P-waves ranges from 9 to 5 μm at 150 to 210 mm from source for the spherical cavity experiment with 1.9 gram explosives, and 8 to 4 μm at 150 to 220 mm from source for spherical experiment with 0.8 gram explosives, 35 to 10 μm at 150 to 240 mm from source for the tamped cylindrical cavity experiment with 1.2 gram explosives and 7 to 2 μm at 150 to 190 mm from source for the decoupled cylindrical cavity experiment with 0.24 gram explosives. The step-like pressure model can be used to explain the experimental results on the peak P-wave induced particle displacement versus propagation distance from the explosions in spherical cavities but not in cylindrical cavities. This results demonstrates the cavity geometrical effects on wave pattern. The experimental results from both spherical and cylindrical cavities show that P-wave profiles are similar with each other.
4. More important, the experimental results in both spherical and cylindrical cavities verify the S-waves generated from both shock wave-to-S conversion at cavity wall and crack propagation in rocks. The amplitude of S-waves from shock wave-to-S conversion is from 10 to 27 μm at 150 to 180 mm from source for the spherical experiment with 1.9 gram explosives, 8 to 21 μm at 150 to 180 mm

from source for the spherical experiment with 0.8 gram explosives. The amplitude of S-waves generated by crack propagation is from 9 to 19 μm at 150 to 180 mm from source for the spherical experiment with 1.9 gram explosives, 8 to 19 μm at 150 to 180 mm from source for the spherical experiment with 0.8 gram explosives.

5. A theoretical model (Section 3.3.4) including multi-reverberation and crack propagation is proposed to explain the differences on P-wave induced displacement history between the observed and the step-like pressure model. The P-wave profiles predicted from this model fits the observation qualitatively as shown in Fig. 3.16.

From the results presented above, we believe that the further study of the characteristics of P- and S-wave profiles generated from explosions, shock wave-to-S conversion and crack propagation driven by explosive products may lead to the development of a criterion to discriminate underground chemical explosions from underground nuclear explosions because

1. cracks generated in chemical explosions may be much longer than that in nuclear explosions as shown in Fig. 5.1. Longer crack length will result in both P- and S-waves with more lower frequency components.
2. the conversion of shock wave-to-S wave at cavity wall may only happen in chemical explosions.
3. P-wave profiles contain the informations about cavity size.

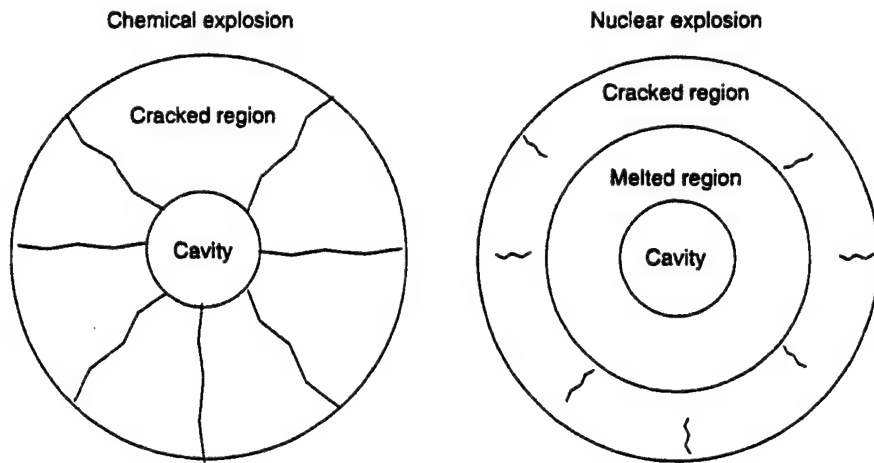


Figure 5.1: Possible damage difference between chemical and nuclear explosions

Acknowledgments

We thank Dr. R. Blandford, AFTAC, for his critical and helpful comments, Dr. Lane Johnson, LBNL, for his help on calculation and Jeff Batten, E. Gelle, M. Long, and V. Nenow for their technical support. We also thank Prof. G. Ravichandran for his advice on crack theory. The project was sponsored by The Air Force Material Command.

Bibliography

- [1] Aki, K. and Richards, P., *Quantitative Seismology Theory and Methods*, W. H. Freeman and Company, 151, 1980.
- [2] Baker, W. E., *Explosion in air*, published by University of Texas Press, Austin, 1973.
- [3] Coursen L., A gas penetration model of fragmentation, *Fragmentation by Blasting*, edited by Fourney W., Boade R. and Costin L., Society for Experimental Mechanics, Connecticut, 1-10, 1985.
- [4] Denny M. and Goodman D., A case study of the seismic source function: Salmon and Sterling reevaluated, *J. Geophys. Res.*, 95, 19,705-19,723, 1990.
- [5] Denny M. and Johnson L., The explosion seismic function: models and scaling laws reviewed, *Explosion Source Phenomenology*, edited by Taylor S., Patterson H. and Richards P., American Geophysical Union, 1-24, 1991.
- [6] Dobratz, B. M., Lawrence Livermore National Laboratory Report, UCRL-51319, 1974.
- [7] Florence A., Miller S. and Keller C., Decoupling of underground explosions by rubble-filled cavities, *J. Geophys. Res.*, 98, 14,197-14,209, 1993.
- [8] Freund, L. B., *Dynamic Fracture Mechanics*, Cambridge University Press, 336-340, 1990.
- [9] Glenn L., Energy-density effects on seismic decoupling, *J. Geophys. Res.*, 98, 1933-1942, 1993.
- [10] Glenn L. and Goldstein P., Seismic decoupling with chemical and nuclear explosions in salt, *J. Geophys. Res.*, 99, 11,732 - 11,730, 1994.
- [11] Glenn L. and Goldstein P., Reply, *J. Geophys. Res.*, 101, 851-854, 1996.

- [12] Glenn L., Ladd A., Moran B., and Wilson K., Elastic radiation from explosively loaded ellipsoidal cavities in an unbounded medium, *Geophys. J. R. astr. Soc.*, 81, 231- 241, 1985.
- [13] Jaeger J. C. and Cook N. G. W., *Fundamentals of Rock Mechanics*, published by Chapman and Hall, London, p 146, 1979.
- [14] Kim S., Clifton R. and Kumar P., A combined normal and transverse displacement interferometer, *J. Appl. Phys.*, 48, 4132-4139, 1977.
- [15] Kanamori H., Mechanic of earthquakes, *Annu. Rev. Earth Planet. Sci.*, 22, 207-237, 1994.
- [16] Klopp, R. W., A. L. Florence and J. K. Gran, Spherical wave interaction with cylindrical holes in large limestone specimens, in *International Conference on Mechanical and Physical Behavior of Materials under Dynamic Loading*, edited by Harding J., Les Editions de Physique, Les Ulis, 735-740, 1994.
- [17] Langston C., Kinematic analysis of strong motion P and SV waves from the Sterling event, *J. Geophys. Res.*, 88, 2486-3497, 1983.
- [18] Lay T. and T. C. Wallace, *Modern Global Seismology*, published by Academic Press, San Diego, 109, 1995.
- [19] Liu, C. and T. J. Ahrens, Shear wave generation from confined explosions in rocks, in *Proc. of Topical Conference on Shock compression of Condensed Matter*, in press, edited by S. C. Schmidt, American Institute of Physics, 1997.
- [20] Masse R., Reviews of seismic source models for underground nuclear explosions, *Bull. Seism. Soc. Am.*, 71, 1249-1268, 1981.
- [21] Murphey B., Particle motions near explosions in Halite, *J. Geophys. Res.*, 66, 947-957, 1961.
- [22] Murphy J. , Types of seismic events and their source descriptions, *Monitoring a Comprehensive Test Ban Treaty*, edited by Husebye and Dainty, Kluwer Academic Publishers, the Netherlands, 247-293, 1996.

- [23] Murphy J., Rimer N. and Stevens J., Comment on " Seismic decoupling with chemical and nuclear explosions in salt" by L. Glenn and P. Goldstein, *J. Geophys. Res.*, 101, 845-850, 1996.
- [24] Rubin, A. M. and T. J. Ahrens, Dynamic tensile-fracture-induced velocity deficits in rock, *Geophysical Research Letters*, 18, 219-222, 1991.
- [25] Sykes L., Dealing with decoupled nuclear explosions under a comprehensive test ban treaty, *Monitoring a Comprehensive Test Ban Treaty*, edited by Husebye and Dainty, Kluwer Academic Publishers, the Netherlands, 225-245, 1996.
- [26] Timoshenko, S. P. and J. N. Goodier, Theory of Elasticity, pp510-513, published by McGraw-Hill Book Company, 1970.
- [27] Walter W., Mayeda K. and Patton H., Phase and spectral ratio discrimination between NTS earthquakes and explosions. Part I: empirical observation, *Bull. Seism. Soc. Am.*, 85, 1050-1067, 1995.

DISTRIBUTION

THOMAS AHRENS
SEISMOLOGICAL LABORATORY 252-21
CALIFORNIA INST. OF TECHNOLOGY
PASADENA, CA 91125

AIR FORCE RESEARCH LABORATORY
ATTN: VSOT
29 RANDOLPH ROAD
HANSOM AFB, MA 01731-3010 (2 COPIES)

AIR FORCE RESEARCH LABORATORY
ATTN: RESEARCH LIBRARY/TL
5 WRIGHT STREET
HANSOM AFB, MA 01731-3004

AIR FORCE RESEARCH LABORATORY
ATTN: AFRL/SUL
3550 ABERDEEN AVE SE
KIRTLAND AFB, NM 87117-5776 (2 COPIES)

RALPH ALEWINE
NTPO
1901 N. MOORE STREET, SUITE 609
ARLINGTON, VA 22209

DOUGLAS BAUMGARDT
ENSCO INC.
5400 PORT ROYAL ROAD
SPRINGFIELD, VA 22151

MUAWIA BARAZANGI
INSTOC
3126 SNEE HALL
CORNELL UNIVERSITY
ITHACA, NY 14853

WILLIAM BENSON
NAS/COS
ROOM HA372
2001 WISCONSIN AVE. NW
WASHINGTON DC 20007

THERON J. BENNETT
MAXWELL TECHNOLOGIES
11800 SUNRISE VALLEY
SUITE 1212
RESTON, VA 22091

ROBERT BLANDFORD
AFTAC
1300 N. 17TH STREET
SUITE 1450
ARLINGTON, VA 22209-2308

JONATHAN BERGER
UNIV. OF CALIFORNIA, SAN DIEGO
SCRIPPS INST. OF OCEANOGRAPHY IGPP, 0225
9500 GILMAN DRIVE
LA JOLLA, CA 92093-0225

CENTER FOR MONITORING RESEARCH
ATTN: LIBRARIAN
1300 N. 17th STREET, SUITE 1450
ARLINGTON, VA 22209

LESLIE A. CASEY
DEPT. OF ENERGY/NN-20
1000 INDEPENDENCE AVE. SW
WASHINGTON DC 20585-0420

ANTON DAINTY
DTRA/OST
45045 AVIATION DRIVE
DULLES, VA 20166-7517

FRANCESCA CHAVEZ
LOS ALAMOS NATIONAL LAB
P.O. BOX 1663, MS-D460
LOS ALAMOS, NM 87545 (5 COPIES)

DIANE DOSER
DEPT. OF GEOLOGICAL SCIENCES
THE UNIVERSITY OF TEXAS AT EL PASO
EL PASO, TX 79968

CATHERINE DE GROOT-HEDLIN
UNIV. OF CALIFORNIA, SAN DIEGO
IGPP
8604 LA JOLLA SHORES DRIVE
SAN DIEGO, CA 92093

MARK D. FISK
MISSION RESEARCH CORPORATION
735 STATE STREET
P.O. DRAWER 719
SANTA BARBARA, CA 93102-0719

DTIC
8725 JOHN J. KINGMAN ROAD
FT BELVOIR, VA 22060-6218 (2 COPIES)

HENRY GRAY
SMU STATISTICS DEPARTMENT
P.O. BOX 750302
DALLAS, TX 75275-0302

I. N. GUPTA
MULTIMAX, INC.
1441 MCCORMICK DRIVE
LARGO, MD 20774

DAVID HARKRIDER
BOSTON COLLEGE
24 MARTHA'S PT. RD.
CONCORD, MA 01742

THOMAS HEARN
NEW MEXICO STATE UNIVERSITY
DEPARTMENT OF PHYSICS
LAS CRUCES, NM 88003

MICHAEL HEDLIN
UNIVERSITY OF CALIFORNIA, SAN DIEGO
SCRIPPS INST. OF OCEANOGRAPHY
9500 GILMAN DRIVE
LA JOLLA, CA 92093-0225

DONALD HELMBERGER
CALIFORNIA INST. OF TECHNOLOGY
DIV. OF GEOL. & PLANETARY SCIENCES
SEISMOLOGICAL LABORATORY
PASADENA, CA 91125

EUGENE HERRIN
SOUTHERN METHODIST UNIVERSITY
DEPT. OF GEOLOGICAL SCIENCES
DALLAS, TX 75275-0395

ROBERT HERRMANN
ST. LOUIS UNIVERSITY
DEPT. OF EARTH & ATMOS. SCIENCES
3507 LACLEDE AVENUE
ST. LOUIS, MO 63103

VINDELL HSU
HQ/AFTAC/TTR
1030 S. HIGHWAY A1A
PATRICK AFB, FL 32925-3002

RONG-SONG JIH
DTRA/PMA
45045 AVIATION DRIVE
DULLES, VA 20166-7517

THOMAS JORDAN
MASS. INST. OF TECHNOLOGY
BLDG 54-918
CAMBRIDGE, MA 02139

LAWRENCE LIVERMORE NAT'L LAB
ATTN: TECHNICAL STAFF (PLS ROUTE)
PO BOX 808, MS L-208
LIVERMORE, CA 94551

LAWRENCE LIVERMORE NAT'L LAB
ATTN: TECHNICAL STAFF (PLS ROUTE)
PO BOX 808, MS L-205
LIVERMORE, CA 94551

LAWRENCE LIVERMORE NAT'L LAB
ATTN: TECHNICAL STAFF (PLS ROUTE)
PO BOX 808, MS L-200
LIVERMORE, CA 94551

THORNE LAY
UNIV. OF CALIFORNIA, SANTA CRUZ
EARTH SCIENCES DEPARTMENT
EARTH & MARINE SCIENCE BUILDING
SANTA CRUZ, CA 95064

ANATOLI L. LEVSHIN
DEPARTMENT OF PHYSICS
UNIVERSITY OF COLORADO
CAMPUS BOX 390
BOULDER, CO 80309-0309

JAMES LEWKOWICZ
WESTON GEOPHYSICAL CORP.
325 WEST MAIN STREET
NORTHBORO, MA 01532

LOS ALAMOS NATIONAL LABORATORY
ATTN: TECHNICAL STAFF (PLS ROUTE)
PO BOX 1663, MS D460
LOS ALAMOS, NM 87545

LOS ALAMOS NATIONAL LABORATORY
ATTN: TECHNICAL STAFF (PLS ROUTE)
PO BOX 1663, MS F665
LOS ALAMOS, NM 87545

LOS ALAMOS NATIONAL LABORATORY
ATTN: TECHNICAL STAFF (PLS ROUTE)
PO BOX 1663, MS C335
LOS ALAMOS, NM 87545

GARY MCCARTOR
SOUTHERN METHODIST UNIVERSITY
DEPARTMENT OF PHYSICS
DALLAS, TX 75275-0395

KEITH MC LAUGHLIN
CENTER FOR MONITORING RESEARCH
SAIC
1300 N. 17TH STREET, SUITE 1450
ARLINGTON, VA 22209

RICHARD MORROW
USACDA/IVI
320 21ST STREET, N.W.
WASHINGTON DC 20451

JAMES NI
NEW MEXICO STATE UNIVERSITY
DEPARTMENT OF PHYSICS
LAS CRUCES, NM 88003

OFFICE OF THE SECRETARY OF DEFENSE
DDR&E
WASHINGTON DC 20330

PACIFIC NORTHWEST NAT'L LAB
ATTN: TECHNICAL STAFF (PLS ROUTE)
PO BOX 999, MS K5-12
RICHLAND, WA 99352

KEITH PRIESTLEY
DEPARTMENT OF EARTH SCIENCES
UNIVERSITY OF CAMBRIDGE
MADINGLEY RISE, MADINGLEY ROAD
CAMBRIDGE, CB3 0EZ UK

DELAINE REITER
WESTON GEOPHYSICAL CORP.
73 STANDISH ROAD
WATERTOWN, MA 0472

MICHAEL RITZWOLLER
DEPARTMENT OF PHYSICS
UNIVERSITY OF COLORADO
CAMPUS BOX 390
BOULDER, CO 80309-0309

CHANDAN SAIKIA
WOODWARD-CLYDE FED. SERVICES
566 EL DORADO ST., SUITE 100
PASADENA, CA 91101-2560

BRIAN MITCHELL
DEPARTMENT OF EARTH & ATMOSPHERIC SCIENCES
ST. LOUIS UNIVERSITY
3507 LACLEDE AVENUE
ST. LOUIS, MO 63103

JOHN MURPHY
MAXWELL TECHNOLOGIES
11800 SUNRISE VALLEY DRIVE
SUITE 1212
RESTON, VA 22091

ROBERT NORTH
CENTER FOR MONITORING RESEARCH
1300 N. 17th STREET, SUITE 1450
ARLINGTON, VA 22209

JOHN ORCUTT
INST. OF GEOPH. & PLANETARY PHYSICS
UNIV. OF CALIFORNIA, SAN DIEGO
LA JOLLA, CA 92093

DAVID RUSSELL
HQ AFTAC/TT
1030 S. HIGHWAY A1A
PATRICK AFB, FL 32925-3002

JAY PULLI
BBN SYSTEMS AND TECHNOLOGIES, INC.
1300 NORTH 17TH STREET
ROSSLYN, VA 22209

PAUL RICHARDS
COLUMBIA UNIVERSITY
LAMONT-DOHERTY EARTH OBSERV.
PALISADES, NY 10964

RICK SCHULT
HQ AFTAC/TTR
1030 SOUTH HIGHWAY A1A
PATRICK AFB, FL 32925-3002

SANDIA NATIONAL LABORATORY
ATTN: TECHNICAL STAFF (PLS ROUTE)
DEPT. 5704
MS 0979, PO BOX 5800
ALBUQUERQUE, NM 87185-0979

SANDIA NATIONAL LABORATORY
ATTN: TECHNICAL STAFF (PLS ROUTE)
DEPT. 9311
MS 1159, PO BOX 5800
ALBUQUERQUE, NM 87185-1159

SANDIA NATIONAL LABORATORY
ATTN: TECHNICAL STAFF (PLS ROUTE)
DEPT. 5736
MS 0655, PO BOX 5800
ALBUQUERQUE, NM 87185-0655

AVI SHAPIRA
SEISMOLOGY DIVISION
IPRG
P.O.B. 2286 NOLON 58122 ISRAEL

MATTHEW SIBOL
ENSCO, INC.
445 PINEDA CT.
MELBOURNE, FL 32940

JEFFRY STEVENS
MAXWELL TECHNOLOGIES
8888 BALBOA AVE.
SAN DIEGO, CA 92123-1506

TACTEC
BATTELLE MEMORIAL INSTITUTE
505 KING AVENUE
COLUMBUS, OH 43201 (FINAL REPORT)

LAWRENCE TURNBULL
ACIS
DCI/ACIS
WASHINGTON DC 20505

FRANK VERNON
UNIV. OF CALIFORNIA, SAN DIEGO
SCRIPPS INST. OF OCEANOGRAPHY
9500 GILMAN DRIVE
LA JOLLA, CA 92093-0225

RU SHAN WU
UNIV. OF CALIFORNIA, SANTA CRUZ
EARTH SCIENCES DEPT.
1156 HIGH STREET
SANTA CRUZ, CA 95064

JAMES E. ZOLLWEG
BOISE STATE UNIVERSITY
GEOSCIENCES DEPT.
1910 UNIVERSITY DRIVE
BOISE, ID 83725

SANDIA NATIONAL LABORATORY
ATTN: TECHNICAL STAFF (PLS ROUTE)
DEPT. 5704
MS 0655, PO BOX 5800
ALBUQUERQUE, NM 87185-0655

THOMAS SERENO JR.
SAIC
10260 CAMPUS POINT DRIVE
SAN DIEGO, CA 92121

ROBERT SHUMWAY
410 MIRAK HALL
DIVISION OF STATISTICS
UNIVERSITY OF CALIFORNIA
DAVIS, CA 95616-8671

DAVID SIMPSON
IRIS
1200 NEW YORK AVE., NW
SUITE 800
WASHINGTON DC 20005

BRIAN SULLIVAN
BOSTON COLLEGE
INSTITUTE FOR SPACE RESEARCH
140 COMMONWEALTH AVENUE
CHESTNUT HILL, MA 02167

NAFI TOKSOZ
EARTH RESOURCES LABORATORY
M.I.T.
42 CARLTON STREET, E34-440
CAMBRIDGE, MA 02142

GREG VAN DER VINK
IRIS
1200 NEW YORK AVE., NW
SUITE 800
WASHINGTON DC 20005

TERRY WALLACE
UNIVERSITY OF ARIZONA
DEPARTMENT OF GEOSCIENCES
BUILDING #77
TUCSON, AZ 85721

JIAKANG XIE
COLUMBIA UNIVERSITY
LAMONT DOHERTY EARTH OBSERV.
ROUTE 9W
PALISADES, NY 10964